Quantifying the Relationship between Embedded Rotation and Extreme Rainfall Rates in Observations of Tropical Storm Imelda (2019)

ALEXANDRA C. MAZUREK[a] AND RUSS S. SCHUMACHER[a]

[a] *Department of Atmospheric Science, Colorado State University, Fort Collins, Colorado*

(Manuscript received 22 April 2022, in final form 14 December 2022)

ABSTRACT: Previous work on continental convective systems has indicated that there is a positive relationship between short-term rainfall rates and storm-scale to mesoscale rotation. However, little has been done to explore this relationship in dense observing networks or in landfalling tropical cyclone (LTC) environments. In an effort to quantify the relationship between rainfall rates and embedded rotation of this scale, we use several sets of observations that were collected during Tropical Storm Imelda (2019). First, a meteorological overview of the event is presented, and the ingredients that led to its flash flood–producing rainfall are discussed. Then, two analyses that investigate the relationship between rainfall rates and storm-scale to mesoscale rotation in the LTC remnants are examined. The first method relies on products from the Multi-Radar Multi-Sensor system, where two spatial averaging approaches are applied to the 0–2-km accumulated rotation track and gauge bias-corrected quantitative precipitation estimate products over hourly time periods. Using these fields as proxies for rotation and rain rates, the results show a positive spatiotemporal relationship between the two products. The second method time matches subjectively identified radar-based rotation and 5-min surface rain gauge observations. There, we show that nearly twice the amount of rain was recorded by the gauges when storm-scale to mesoscale rotation was present nearby, and the differences in 5-min rainfall observations between when rotation was present versus not was statistically significant. Together, these results indicate that more rain tended to fall in locations where there was rotation embedded in the system.

SIGNIFICANCE STATEMENT: Tornadoes and flash floods frequently occur in unison over the same locations, which can complicate forecasting, warning, and communication efforts within the meteorology community. Previous work has furthered the understanding of the interconnectedness of these hazards by suggesting a relationship between two of their predecessors: storm rotation and rainfall rates. We build on this research by quantifying the relationship of these two processes using observations from Tropical Storm Imelda: a system that brought devastating flooding to southeast Texas in September 2019. Our results show across multiple observational datasets that more rain tended to fall in locations where there was rotation embedded in the tropical storm remnants.

KEYWORDS: Flood events; Rainfall; Tropical cyclones

1. Introduction

Tornadoes and flash floods (TORFFs) can be deadly hazards on their own (Ashley 2007; Ashley and Ashley 2008), but what happens when they occur concurrently over the same locations? It is a threat that occurs somewhat frequently, with an average of 400 TORFF warning overlaps occurring each year in the contiguous United States (CONUS) (Nielsen et al. 2015). These situations complicate the forecasting process for meteorologists, as environments that produce TORFFs often share meteorological characteristics with patterns that are favorable for only one of the two hazards (e.g., Rogash and Racy 2002; Nielsen et al. 2015). Further, monitoring flash flooding and tornadoes simultaneously can divide forecaster attention, potentially leading to one threat being focused on over the other during warning operations (Henderson et al. 2020). For these reasons, understanding the relationships among the processes that lead to concurrence of these phenomena is crucial.

The definition for what qualifies as a concurrent TORFF event has varied some across the literature. While some work has studied these overlapping hazards on the system-scale (e.g., Rogash and Smith 2000; Schumacher and Johnson 2006), other studies have suggested more explicit definitions by constraining the time and distance over which the tornado and flash flood must occur. For example, Rogash and Racy (2002) provided one of the first attempts at classifying these events by requiring at least one F3+ or two F2 tornadoes to occur within 250 km and ±3 h of "significant flash flood reports … in at least three counties" (p. 156). More recently, Nielsen et al. (2015) offered an even narrower definition by characterizing a TORFF event as the collocation of a confirmed tornado path and flash flood observation within a 3-h time period. The same study also coined the overlap of a storm-based tornado warning and flash flood warning within a 30-min time frame as a TORFF event—a definition that has been applied in recent studies on of forecasting practices (Henderson et al. 2020) and tropical cyclone (TC) environments (Burow et al. 2021).

Supplemental information related to this paper is available at the Journals Online website: https://doi.org/10.1175/MWR-D-22-0115.s1.

Corresponding author: Alexandra Mazurek, Allie.Mazurek@colostate.edu

DOI: 10.1175/MWR-D-22-0115.1

Though previous work has identified broad, synoptic-scale environments that are favorable for producing TORFFs (e.g., Rogash and Smith 2000; Rogash and Racy 2002; Schumacher and Johnson 2006; Nielsen et al. 2015) insights on predecessors to individual TORFF events can be attained by focusing on the storm scale. Early discussions surrounding this topic have begun with supercell thunderstorms—a convective mode frequently associated with tornadogenesis or other severe hazards, though considered far less often for their flash flood potential (e.g., Doswell 1998). This notion that supercells do not produce heavy rainfall is not necessarily incorrect, as they often have fast translational speeds (e.g., Doswell 1998; Smith et al. 2001) and small precipitation footprints (when in the form of discrete cells, rather than embedded within a larger convective system). Despite these typical characteristics, supercells are capable of producing locally heavy rainfall, often over time spans as short as an hour or less (Doswell 1998; Smith et al. 2001; Hitchens and Brooks 2013; Bluestein et al. 2015; Brauer et al. 2020; Nielsen and Schumacher 2020a).

Additional investigations of storm dynamics have underscored how rotating updrafts in supercells may contribute to heavy rainfall. Observations have shown that supercells can have intense upward vertical velocities (e.g., Marinescu et al. 2020)—a quantity that is directly proportional to rain rate (R) as shown by Doswell et al. (1996):

$$R = Ewq, \tag{1}$$

where E is precipitation efficiency, w is the vertical ascent rate, and q is the ambient water vapor mixing ratio. To expand on this idea, Nielsen and Schumacher (2018) showed that as increasing vertical wind shear enhances low-level mesoscale rotation, the nonlinear dynamic component of the vertical perturbation pressure gradient force increases (indicating enhanced upward motion), which allows parcels that would have been otherwise stable to be lifted to saturation. Referring back to Eq. (1), it is logical that this process would create a more favorable environment for higher rain rates, as both w and q should theoretically increase, which would increase R as a result. The positive relationship between mesoscale rotation and locally heavy rainfall rates has also been corroborated with observations on hourly time scales in continental systems (Nielsen and Schumacher 2020a).

On the larger system scale, it is well documented that landfalling tropical cyclones (LTCs) can be prolific rain producers. With regards to precipitation, system speed is the primary driver of the excessive rainfall in LTCs, as the slowest-moving LTCs tend to have a greater maximum storm-total rainfall (DeHart and Bell 2020; Galarneau and Zeng 2020). However, as is supported by Eq. (1), moisture content and precipitation efficiency also play a significant role in rainfall production in LTCs. For instance, Galarneau and Zeng (2020) documented that relative to a 40-yr climatology of CONUS LTCs, the heaviest rain-producing LTCs tended to have above-average area-mean precipitable water that was sustained for several days post-landfall. Additionally, enhanced warm rain processes and high-concentration drop size distributions have been documented with LTCs—both of which can positively contribute to precipitation efficiency (Brauer et al. 2020; DeHart and Bell 2020). Strongly sheared environments that lead to rapidly decaying LTCs can also support more well-organized convection (e.g., Corbosiero and Molinari 2002) and assist with greater precipitation production (e.g., DeHart and Bell 2020).

While understanding the linkages between LTC precipitation and system-wide dynamics in the production of extreme rainfall is crucial, some previous work has also highlighted the role of smaller, more localized dynamics—including meso- and storm-scale processes—for LTC rainfall. Because LTCs are often responsible for creating "hybrid" flooding—consisting of both flash and slow-rise flooding—(Dougherty and Rasmussen 2019) there is reason to believe that multiscale flood-producing processes exist across the system, such as when supercells are embedded in the tropical rainbands. Recent work by Brauer et al. (2020) demonstrated that in Hurricane Harvey (2017), supercell-style mesoscale rotation was collocated with locally heavy rainfall—suggesting that these smaller scale dynamics are important. However, their study did not quantify the contributions of individual embedded supercells to localized rainfall rates, and most other research on supercells in LTCs has focused on tornadogenesis processes (e.g., McCaul 1987, 1991; McCaul and Weisman 1996; Spratt et al. 1997; Green et al. 2011; Edwards 2012; Edwards et al. 2012, 2018; Nowotarski et al. 2021) rather than their ability to produce localized extreme rainfall rates. Since TORFF events can occur frequently in LTCs (Burow et al. 2021; Nielsen et al. 2015), there is motivation to further investigate the interconnectivity between heavy rainfall and tornado-producing processes in these environments.

Thus, our study aims to better understand the significance of the relationship between heavy precipitation rates and embedded rotation (which can be a precursor to tornadogenesis) in an LTC environment—an area that has yet to be thoroughly investigated. To do this, we use several observational datasets with fine spatiotemporal resolutions in an effort to quantify the differences in precipitation when embedded meso- to storm-scale rotation is present versus when it is not. We use Tropical Storm Imelda as the case for our investigation: a system that had significant impacts on the western U.S. Gulf Coast in September 2019. In section 2, a synoptic and mesoscale analysis of this LTC is presented, and the multiscale factors that contributed to its exceptional rainfall are highlighted. Section 3 details the datasets and methods that are used to examine embedded rotation and rainfall rates in the LTC. Section 4 outlines the results of the analyses, and section 5 provides conclusions and avenues for future work.

2. Meteorological overview of Tropical Storm Imelda

Tropical Storm Imelda impacted the western Gulf Coast for several days in September 2019. Despite being a named TC for only a short time, the slow-moving system brought several days of flood-producing heavy rain and a couple of tornadoes to southeast Texas and southern Louisiana (Fig. 1). During the time leading up to its landfall and the day or so after, Imelda displayed characteristics similar to most weak TCs, such as spiraling rainbands with locally heavy precipitation and an isolated tornado risk. However, as Imelda's

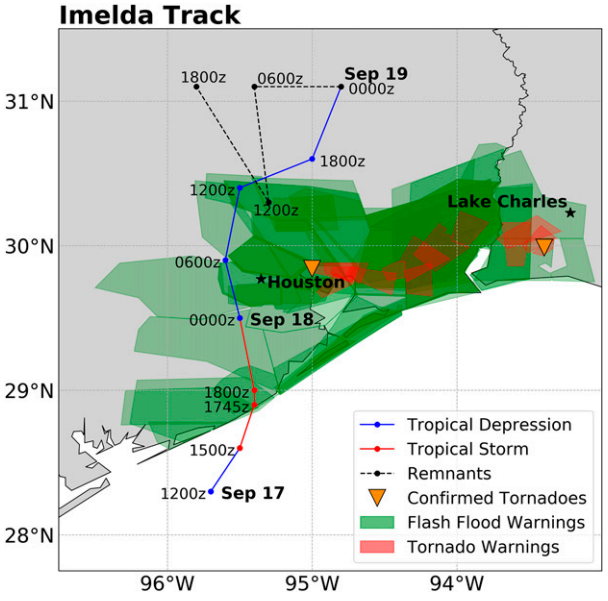

FIG. 1. Tropical Storm Imelda track from the time at which it became a named tropical storm to its dissipation using National Hurricane Center HURDAT2 best track data (1800 UTC 23 Aug–1200 UTC 2 Sep) (Landsea and Franklin 2013) and Weather Prediction Center (WPC) surface analysis data (0000–1800 UTC 19 Sep). Location of remnants are estimated from low pressure center locations on WPC surface maps. Dates and times are also annotated. Green polygons indicate Imelda-related storm-based flash flood warnings and red polygons indicate Imelda-related storm-based tornado warnings (archived warnings courtesy of Iowa Environmental Mesonet). Confirmed tornadoes are shown as orange triangular markers based on data from the NCEI Storm Events Database (NOAA/National Centers for Environmental Information 2021a).

structure deteriorated over land, the remnants of the system transformed into a quasi-stationary back-building convective line with embedded rotation that brought extreme rainfall rates in excess of 100 mm h^{-1} to some already saturated areas, which led to flooding. This interesting transformation provided motivation for the case study.

a. *System evolution*

Tropical Storm Imelda's origin can be traced back to an area of weak mid- to upper-level cyclonic circulation off the coast of the southeastern United States—separate from the more prominent trough–ridge pattern to the north—that began around 9 September. The upper-level low drifted southwestward across the Florida peninsula into the eastern Gulf of Mexico as it intensified slightly (Latto and Berg 2020). Embedded in a weak flow regime, the cyclonic feature continued drifting westward, remaining rather lackluster from an organizational standpoint. The system finally became surface based by 1200 UTC 16 September, as indicated by buoy data off the Texas coast. Other than some showers, precipitation remained primarily offshore until the following day as the low drifted closer to shore (see Supplemental Fig. 1 for a full radar reflectivity loop of the event). By 1200 UTC 17 September, the system became better organized and was named Tropical Depression 11 while TC-like rainbands spiraled inland. The low pressure system was upgraded to tropical storm status by 1500 UTC on the same day, then proceeded to make landfall at its peak intensity [1003-hPa surface pressure with maximum sustained winds of 40 kt (1 kt ≈ 0.51 m s^{-1})] less than 3 h later near Freeport, Texas (Fig. 1).

Soon after Imelda's landfall, thunderstorm activity gradually became more widespread in the afternoon of 17 September as it slowly moved inland (Fig. 2a). The TC quickly weakened to a depression by 0000 UTC 18 September as precipitation persisted, with the majority of the heaviest rainfall being concentrated on the south–southeast side of the system relative to its center of circulation (Fig. 2b). As the remnant low meandered northward, additional areas of intense precipitation continued to push onshore (Fig. 2c).

By 0000 UTC 19 September, widespread rainfall totals in excess of a few hundred millimeters had already fallen across the western Gulf Coast region (according to estimates from the Multi-Radar Multi-Sensor system) as an area of cloud tops began to rapidly cool south of the remnant TC's center of circulation. This feature was associated with a north–south-oriented convective line that was located just west of the Texas–Louisiana border (Fig. 2d). By 0330 UTC, small convective cells began to develop just west of this precipitating feature, which propagated eastward in a linear fashion as new cells continued to develop upstream relative to their direction of propagation (Fig. 2e). This west-northwest–east-southeast-oriented convective line consisting of merging and back-building cells intensified over the next few hours, eventually developing a "t-shaped" structure (Fig. 2f). Additionally, embedded rotating features on the meso- to storm-scales became established within the system. This quasi-stationary, back-building mesoscale convective system (MCS) persisted for at least another 6 h, bringing rainfall rates that were at times in excess of 100 mm h^{-1} (Fig. 2g).

After approximately 12 h of near-stationary behavior, the linear band of intense precipitation finally began to bow and progress southwestward by around 1400 UTC (Fig. 2h), bringing it into Harris County and the greater Houston metropolitan area. The system gradually became weaker and less organized over the next few hours (Fig. 2i), eventually devolving into scattered thunderstorms by 2200 UTC. While flooding persisted, precipitation had largely concluded in southeast Texas and southern Louisiana on 20 September, though the remnants of the system did bring some heavy rainfall to southeast Oklahoma (Latto and Berg 2020) before finally dissipating.

b. *Processes supporting extreme rainfall*

There were a number of factors that contributed to the heavy rainfall rates caused by Imelda's remnants on 19 September including moisture availability, instability, and low-level wind behavior. Observed sounding profiles from Lake Charles, Louisiana (Figs. 3a–c), show that throughout 19 September, when the greatest amounts of rain fell, a deep unstable layer was maintained, with the largest values present during the local morning hours

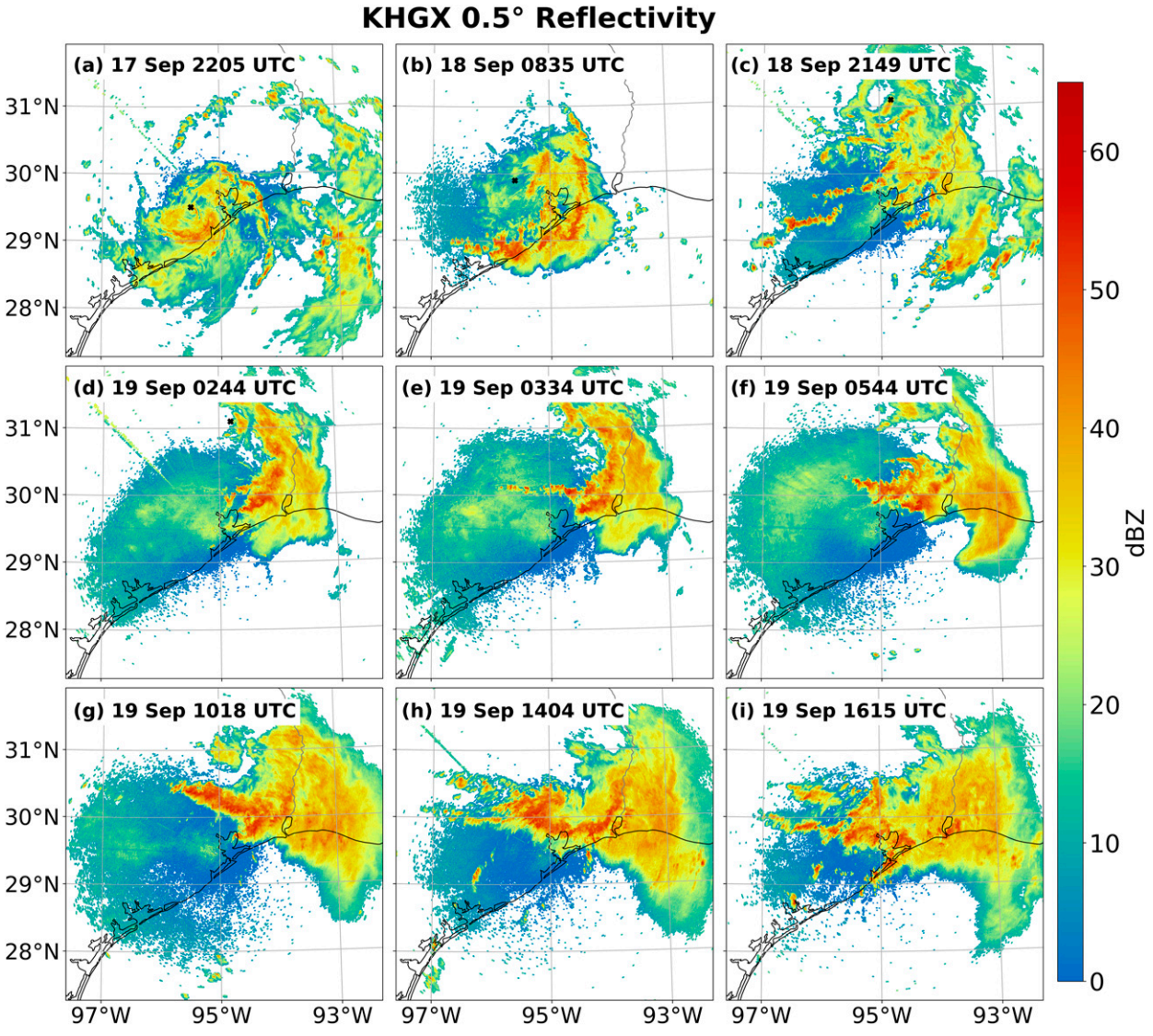

FIG. 2. The 0.5° radar reflectivity from the Houston–Galveston radar in League City, TX (KHGX), at (a) 2205 UTC 17 Sep; at (b) 0835 and (c) 2149 UTC 18 Sep; and at (d) 0244, (e) 0334, (f) 0544, (g) 1018, (k) 1404, and (i) 1615 UTC 19 Sep. In (a)–(d), the black "x" indicates the approximate storm center according to its location at the 6-h time stamp from the HURDAT2 track (shown in Fig. 1) that is nearest to each radar time stamp.

(Fig. 3b). The temperature profiles also show a deep warm layer (with the freezing layer falling between 600 and 700 hPa), signaling a favorable environment for warm rain processes. In terms of moisture content, the soundings illustrate sustained saturation near the surface as well as the midlevels, and column-integrated precipitable water values exceeded 60 mm (Figs. 3 and 4a,b). Meanwhile, a strong gradient in surface temperatures (Figs. 4c,d) and surface-based CAPE (SBCAPE, not shown) resulted from a cold pool generated by differential heating between surfaces under cloudy versus clear skies, which can also be seen in infrared satellite imagery (not shown). Modest dry air in the low levels (Fig. 3a) may have further enhanced this temperature gradient via evaporative cooling. This surface cold pool would ultimately serve as a mechanical lifting mechanism that would enhance precipitation processes.

In terms of dynamics, vertical wind profiles in the soundings indicate a veering wind profile (Fig. 3), which is typically associated with warm air advection and helped sustain moisture-rich air (from the Gulf) over the region. While near-surface winds show that Imelda's low-level circulation had largely dissipated by the start of 19 September (Fig. 4c), cyclonic winds were still present in the low levels (Fig. 4a), as well as the midlevels (not shown). Additionally, two enhanced corridors of low-level winds are apparent at 1200 UTC (Fig. 4b): one from the west, and one from the south. The former appears to be a result of confluent winds from the northwest (associated with the remnant cyclone) and the southeast, while the latter

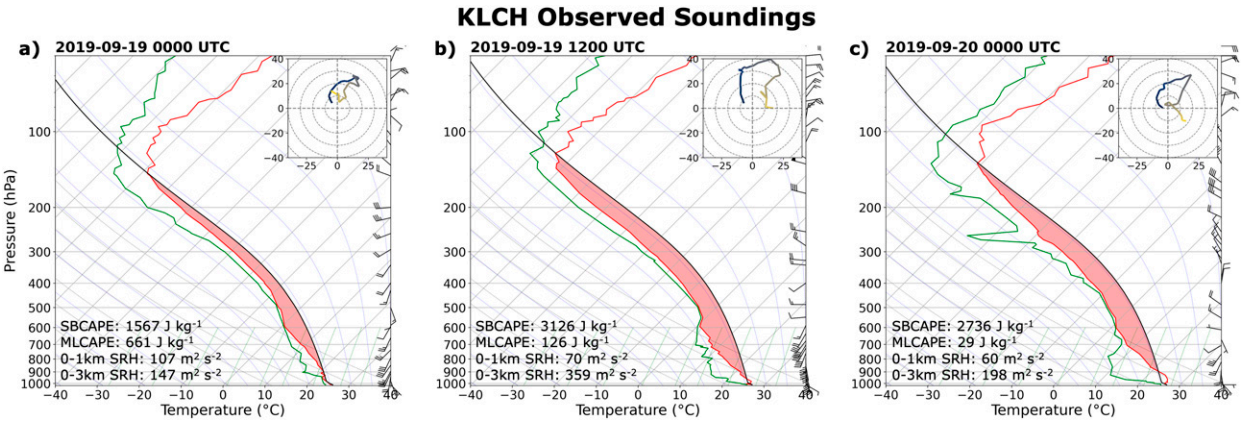

FIG. 3. Observed upper-air soundings and hodographs from Lake Charles, LA (KLCH), for (a) 0000 UTC 19 Sep, (b) 1200 UTC 19 Sep, and (c) 0000 UTC 20 Sep. Parcel trajectories (black line) shown are for surface-based parcels, surface-based convective available potential energy (SBCAPE) is shaded in red, and temperature and dewpoint profiles are shown as red and green lines, respectively. SBCAPE, mixed-layer CAPE (MLCAPE), 0–1-km storm-relative helicity (SRH), and 0–3-km SRH are annotated. Wind barbs and hodographs are shown in units of knots. Sounding data are courtesy of the University of Wyoming sounding archive and are plotted using MetPy (May et al. 2021).

seems to be enhanced at least in part by a synoptic-scale pressure gradient (not shown). This pattern of low-level winds helped provide sufficient vertical shear to support rotating updrafts [see storm-relative helicity (SRH) in Fig. 3b] and thus aided in ascent. Further, this area of enhanced winds impinged perpendicularly on the cold pool that was present throughout much of the period (Fig. 4d)—a mechanism that also may have provided forcing for upward motion, as is

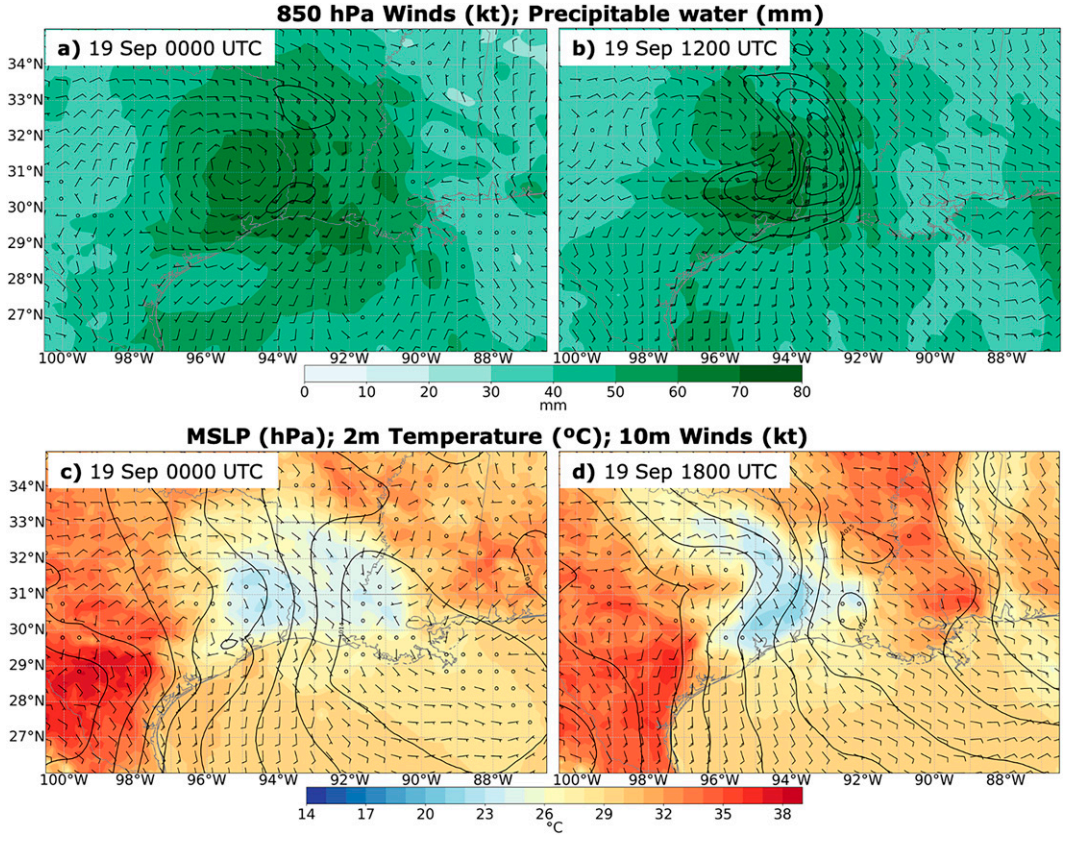

FIG. 4. The 13-km Rapid Refresh (RAP; Benjamin et al. 2016) analysis showing 850-hPa winds (contoured every 5 kt for 25+ kt) and column-integrated precipitable water (fill) for (a) 0000 UTC 19 Sep and (b) 1200 UTC 19 Sep; surface maps showing mean sea level pressure (MSLP) (contoured every 1 hPa), 2-m temperature (fill), and 10-m winds for (c) 0000 UTC 19 Sep and (d) 1800 UTC 19 Sep.

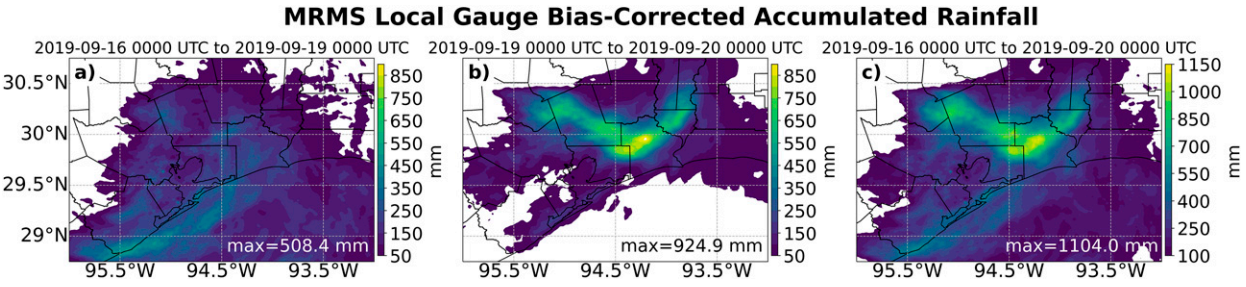

FIG. 5. Multi-Radar Multi-Sensor (MRMS) local gauge bias-corrected quantitative precipitation estimate (QPE) for (a) 0000 UTC 16 Sep–0000 UTC 19 Sep, (b) 0000 UTC 19 Sep–0000 UTC 20 Sep, and (c) 0000 UTC 16 Sep–0000 UTC 20 Sep.

evidenced by the maximum in surface moisture convergence (not shown). Examining the wind shear over a deeper layer (i.e., 850–250 hPa) reveals a southward-oriented shear vector, meaning that the most intense rain fell on the downshear side of the remnant midlevel circulation (not shown). This pattern in the precipitation footprint is consistent with previous work that has examined the ways in which synoptic-scale vertical wind shear can affect precipitation distribution in LTCs (e.g., Gao et al. 2009; Shu et al. 2018). As a whole, Imelda's slow translational speed allowed these heavy rainfall–producing processes to persist over the same locations for many hours.

To summarize, a series of ingredients came together to give way to the heavy rain that fell in association with Imelda's remnants. First, column-integrated moisture values had remained high (despite the system being inland for over 48 h), suggesting that southerly flow in the low levels helped sustain moisture in the area. There was also ample surface-based instability and well-maintained deep warm cloud depths which provided favorable conditions for warm rain processes. Additionally, ongoing precipitation led to a localized temperature gradient, which provided a boundary for low-level confluence from the northwest and southwest to interact with—leading to forcing for ascent. A corridor of enhanced southerly winds also developed to the east of the confluent wind field, which enhanced low-level shear and rising vertical motion on the eastern side of the system. The combination of moderate to high SBCAPE values and relatively high 0–3-km SRH values (as shown in the soundings and hodographs) suggested potential for rotating updrafts (as was evident in several locations within the convective system and will be shown in the storm-relative velocity data in the next section). With the ingredients in place for deep convection, radar imagery showed persistent development of new cells along the western periphery of the east–west-oriented MCS as mature cells propagated eastward, which favored ongoing strong convection to occur over the same locations for several hours. These processes continued throughout much of 19 September until the instability and forcing were no longer collocated, which led to the system's degeneration.

Some environmental characteristics associated with Imelda on 19 September shared similarities to environments described in previous literature on heavy rain-producing MCSs. The presence of enhanced southerly low-level winds intersecting with the decaying midlevel cyclonic circulation (which was the remnants of Imelda in this case) accompanied by high-θ_e air (not shown) to the south and west (that was also being positively advected into the region where the MCS developed) strongly resembled the environmental setup described in Schumacher and Johnson (2009)'s study on quasi-stationary/back-building convection (see their Fig. 13a). Notable differences that were found with Imelda were a more prominent cold pool, and the zone of enhanced low-level westerlies resulting from confluent northwesterly and southwesterly winds, which were features that their results did not show. However, a similar wind field was present in Keene and Schumacher (2013)'s study on "bow and arrow" convection, as were some other features that were evident in Imelda's remnants. Comparing Imelda's fields to their Fig. 25, these similarities include 1) a bowing MCS (the "bow") that preceded the upstream development of the "arrow," 2) a surface cold pool, created by the cool outflow from the bow, 3) enhanced westerly winds that intersected the warm side of the cold pool and provided forcing for ascent, and 4) the subsequent development of the arrow—a linear convective feature that developed along the cold outflow approximately parallel to the bow.

One other case that Imelda presented similarities to was illustrated in Wang et al. (2015), where they showed that an east–west-oriented back-building MCS developed within the rainbands on the south side of a typhoon—perpendicular to a terrain-induced north–south-oriented convective line. This t-shaped zone of convection resembled the structure of Imelda's remnants. Further, their study showed that the quasi-stationary back-building convective line was supported by shear driven by northwesterly winds converging with a westerly low-level jet—wind pattern that suggests another parallel to Imelda. It is important to note, however, that orography also played a significant role in their study, which was not a factor in this case.

c. *Impacts*

The flood-producing rainfall was the primary cause of the damage that resulted from Imelda in southeast Texas. Although the system's slow motion contributed to the heavy precipitation, the extreme rain rates on 19 September were primarily responsible for the rapidly developing flash flood event (Fig. 5). Based on the maximum rainfall that fell with Imelda (approximately 1125 mm), the LTC became the fifth wettest on record to impact CONUS (Weather Prediction Center 2020), surpassing rain totals from other notorious heavy rain–producing systems such as Tropical Storm Allison

(2001) and Hurricane Florence (2018). Imelda's rain totals were lower and covered a smaller geographic area compared to Hurricane Harvey in 2017, though many of the same areas were impacted.

The flood-producing rainfall associated with Tropical Storm Imelda ultimately led to 5 deaths, several high water rescues, and damage to thousands of homes (Latto and Berg 2020). In addition to the flooding caused by Imelda, some additional damage occurred as a result of two brief tornadoes (one rated EF0 and one rated EF1). Economically, Tropical Storm Imelda was classified as a billion-dollar disaster, with damage estimates exceeding $5 billion (U.S. dollars) (NOAA/National Centers for Environmental Information 2021b).

3. Data and methods

Southeast Texas is well-covered by a variety of surface-based observing networks, offering high-quality meteorological data from several sources. Given that surface-based observations are often sparse, this study allows for a somewhat rare opportunity to examine observed concurrent, collocated rotation and rainfall rates on finer spatial and temporal scales than have yet to be explored in the literature. The data and methods employed to investigate this relationship in Tropical Storm Imelda (specifically, during 19 September—when the majority of the rain fell) are detailed below.

a. Multi-Radar Multi-Sensor (MRMS) products

The MRMS system blends data from over 170 radars across CONUS and southern Canada with data sourced from numerical models, satellites, surface observing networks, and more to create a suite of over 30 gridded products (Zhang et al. 2011; Smith et al. 2016; Zhang et al. 2016). This study uses two MRMS products to explore the relationship between rainfall and mesoscale/storm-scale rotation in Tropical Storm Imelda. Specifically, the local gauge bias-corrected 1-h quantitative precipitation estimate (QPE) product (hereafter, MRMS radar-gauge QPE) is used for accumulated rainfall, and the accumulated 60-min 0–2-km rotation track product is used as a proxy for low-level rotation (hereafter, MRMS rotation tracks). The MRMS radar-gauge QPE product has a 1-h temporal resolution, whereas the MRMS rotation tracks are available every 2 min. The products have horizontal grid spacings of 0.01° (~1 km) and 0.005° (~0.5 km), respectively. Additional details on these products can be found in Smith et al. (2016) and Zhang et al. (2016).

While the MRMS system has some limitations, the products should be appropriate to use in this work. One of the benefits to using data from the MRMS system is that the gridded nature of MRMS products provide continuous data for CONUS, effectively filling in the gaps of datasets that are discrete or limited in coverage (e.g., rain gauges or single radars). While interpolation is needed to achieve this continuity, the radar-estimated precipitation used in the MRMS QPE products has performed well relative to surface observations during recent extreme rainfall events in southeast Texas, such as Hurricane Harvey (2017) and the Memorial and Tax Day floods (2015 and 2016, respectively) (Gao et al. 2021). Recent work by Habibi et al. (2021) has shown that the MRMS QPE was strongly correlated with surface observations during Tropical Storm Imelda as well—particularly when accumulations were compared over hourly time scales. Despite its overall positive performance in heavy rainfall events over southeast Texas, the MRMS QPE has been shown to overestimate heavy precipitation rates and underestimate lighter precipitation in the region (Gao et al. 2021; Habibi et al. 2021). And while the formulas for calculating precipitation rates in the MRMS system have become more sophisticated by incorporating additional variables such as specific differential phase (Zhang et al. 2020), the system relied on the much simpler reflectivity-based algorithms (i.e., Z–R relationships) at the time of Imelda (Zhang et al. 2016), which may have contributed to some of these errors. Using the MRMS radar-gauge QPE (as opposed to the radar-only QPE) should help alleviate some of these biases, though it is worth noting that data from many of the gauges in the region are not assimilated into the product (such as most of those that are located in Jefferson County, Texas, where some of the heaviest rain rates occurred during Imelda) (Zhang et al. 2016). In addition to the limitations that exist with the MRMS QPE data, there are some shortcomings of the MRMS rotation track data that should also be taken into account. One limitation that may be relevant to our study is that the MRMS rotation tracks can become difficult to analyze when rotating features intersect each other (such as in back-building convection) during the hourly "accumulation" periods, since the dataset reflects the hourly maximum azimuthal shear values for each grid point in the domain (Smith et al. 2016). In other words, the larger azimuthal shear values from one mesocyclonic rotating feature may mask smaller azimuthal shear values associated with a weaker rotating feature if they intersect within the 1-h period. While Imelda had storm dynamics where these overlaps may be a concern, this analysis is primarily concerned with analyzing the overarching footprints of the MRMS rotation and MRMS QPE on hourly time scales (rather than their behavior across subhourly time frames), so this issue should not affect the goals of this portion of the study.

Despite these limitations, the QPE and rotation track products from the MRMS system should still be reliable given that the region is well-covered by two WSR-88D polarimetric radars: KLCH in Lake Charles, Louisiana, and KHGX in League City, Texas. Because of the close proximity to these sensors, the lower levels of the atmosphere that are of interest in this study are captured well by the lower radar elevation scans, which improves the accuracy of the data. Plus, Imelda's remnants remained nearly stationary for much of the study period, so issues associated with moving between areas with greater and lesser radar coverage are largely avoided.

b. MRMS data analysis methods

Because the MRMS products used in this study—particularly the rotation tracks—are noisy and have a finer horizontal grid spacing than the horizontal extent of the rotation-rainfall rate relationships that are being examined, it is crucial to apply spatial averaging methods to the data. Here, two different spatial

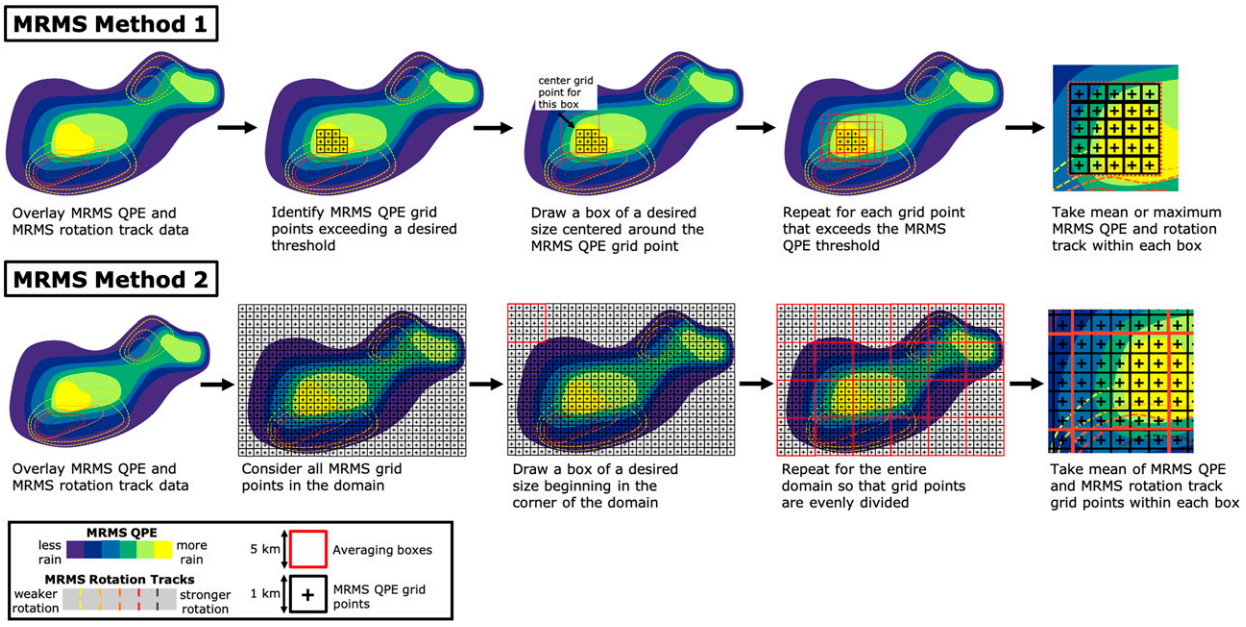

FIG. 6. Idealized schematic demonstrating (a) Multi-Radar Multi-Sensor (MRMS) method 1 and (b) MRMS method 2 as described in the text. MRMS local gauge bias-corrected quantitative precipitation estimate (QPE) is shown as the filled contours, and MRMS 1-h accumulated 0–2-km rotation tracks are shown as dashed contours. Magnitudes of the QPE and rotation are shown in the legend. MRMS local gauge bias-corrected quantitative precipitation estimate grid points (1-km spatial resolution) are indicated by black boxes with crosses, and averaging boxes (shown here for a spatial resolution of approximately 5 km) are indicated by red boxes.

averaging techniques are applied to the MRMS rotation tracks and radar-gauge QPE, with each being examined over 1-h time steps for 0000–1800 UTC 19 September, which is when the highest rain rates occurred (Fig. 5). For both approaches, the two products are overlaid and the averaging method is applied for each 1-h period across a domain extending from approximately 28.5° to 33.0°N and from 92° to 97°W.

The first method (hereafter, MRMS method 1) averages the two datasets for each 1-h period based on an accumulated precipitation threshold within the MRMS radar-gauge QPE product (Fig. 6a) Specifically, all grid points that exceed 32 mm h^{-1} are selected, and a small box is "drawn" around each grid point meeting that criterion. This threshold is used because it is large enough to only target precipitation taking place within the main core of the system, effectively neglecting grid cells with low precipitation rates that are near the edge of the domain, whose averaging boxes would include grid cells outside the domain. All grid points—both for the MRMS radar-gauge QPE and overlaid MRMS rotation tracks—that fall within each averaging box are averaged for each time stamp. Four different averaging box sizes that are mapped to the MRMS Lambert Conformal grid are tested, each of which equate to cartesian areas of approximately 11 km × 12 km, 22 km × 21 km, 33 km × 33 km, and 44 km × 45 km.

MRMS method 1 allows for overlaps in the averaging boxes, which leads to concerns of oversampling the data. To address this matter, the second two-dimensional spatial averaging method (MRMS method 2 hereafter), also uses averaging boxes but does not permit overlaps between them. Rather, the MRMS grid is coarsened independently from the MRMS radar-gauge QPE values by evenly dividing both the precipitation and rotation track grids for each 1-h period using averaging boxes of various sizes (Fig. 6b). The grids are coarsened using box sizes of approximately 2 km × 2 km, 5 km × 5 km, and 10 km × 10 km. For the analysis of MRMS method 2, only averaging boxes with an area-averaged QPE value that exceeded 4 mm and an area-averaged rotation track value that exceeded 0.001 s^{-1} are included, so that very small values of the products are omitted.

The relationship between the MRMS area-averaged radar-gauge QPE and MRMS area-averaged rotation tracks is assessed for each method. To test the statistical significance of the relationship between rainfall and rotation in the MRMS data, 100 random averaging boxes containing the area-averaged MRMS radar-gauge QPE and area-averaged rotation track values are selected. The choice to sample the data rather than use the full population was done because the large size of the population yielded a very large number of degrees of freedom and thus a very small critical value, which would have been meaningless for assessing statistical significance. This random selection of 100 values is repeated 1000 times for each of the four averaging box sizes used in MRMS method 1 and 10 000 times for each of the three averaging box sizes used in MRMS method 2. The number of iterations for randomly selecting the 100 values is somewhat arbitrary, though these numbers of iterations seemed to be sufficient when it came to reproducing the results across multiple random seeds for each MRMS method. For both MRMS methods, a mean critical value is calculated across all iterations. The null hypothesis is that based on the mean critical value, there is no

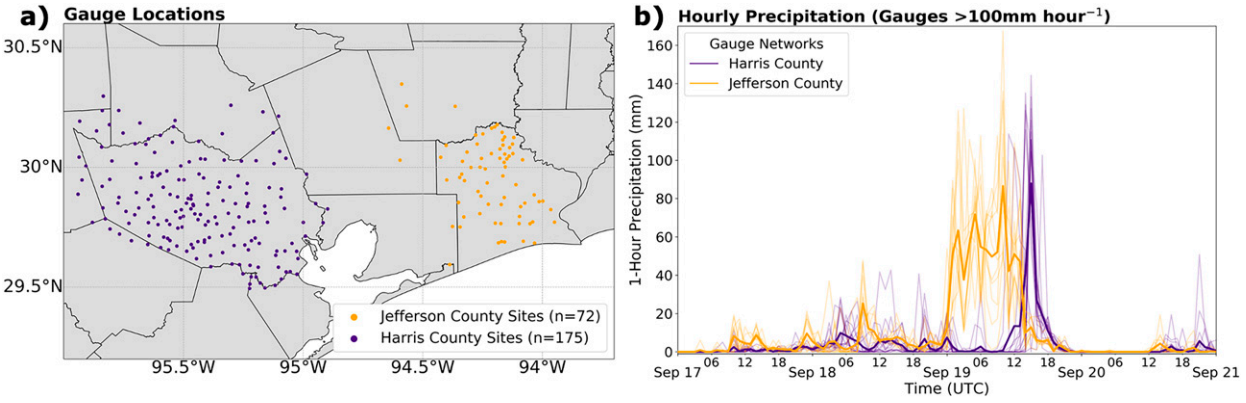

FIG. 7. (a) Locations of rain gauge sites for the Harris County (purple) and Jefferson County (orange) networks and (b) hourly precipitation for networks' gauges that received over 100 mm h^{-1} during at least one hourly period from 0000 UTC 17 Sep to 0000 UTC 21 Sep 2019. Note that in (b) only 60-min periods that begin at the top of an hour and end at the bottom of an hour (e.g., 0500–0600 UTC) are considered. In (b), hourly data from individual gauges are shown as thin lines, and hourly mean data among the individual sites are shown as bolded lines.

correlation between the MRMS radar-gauge QPE and the MRMS rotation tracks.

c. *Polarimetric radar and rain gauge comparison*

There are two dense networks of rain gauge sites in southeast Texas: one in Jefferson County (which includes the city of Beaumont) and one in Harris County (which includes the city of Houston) (Fig. 7a). After filtering out stations reporting erroneous data, the two networks comprise nearly 250 sites that report precipitation observations every 5 min.

As was shown in section two, the most extreme precipitation rates during Imelda took place throughout 19 September, which is also reflected in the hourly rainfall rates[1] of the gauge sites (Fig. 7b). Filtering the data to only include gauges that reported rain rates in excess of 100 mm h^{-1}—a threshold comparable to previous studies that have used high-resolution precipitation datasets (Nielsen and Schumacher 2020a)—Fig. 7b shows that the Jefferson County sites meeting this criteria ($n = 11$) recorded extreme precipitation rates for a longer period than the Harris County sites ($n = 17$). This difference is due to the increased translational speed of the system toward the end of the period. Thus, to capture a longer observation period and maintain similar radar coverage quality among the sites, further analysis is restricted to only the Jefferson County sites.

After collecting the 5-min precipitation data for the 11 gauge sites, the sites are each centered within their own unique domain of size ±0.15° latitude and ±0.17° longitude relative to their geographic coordinates, with each area equating to approximately 33 km × 33 km. This sized area proved to be best suited for monitoring storm-scale rotation after testing larger and smaller areas. Level II reflectivity and storm-relative velocity data from the Houston–Galveston NEXRAD WSR-88D polarimetric radar (KHGX) are then overlaid across each of the 11 domains for the period when the most extreme rainfall rates were reported by the gauges (i.e., 0000–1400 UTC 19 September, Fig. 7b). This process yielded a total of 1067 radar images.

The images are then each paired with their respective gauge observations for all time stamps in the 14-h period. Because the temporal resolution of the radar and gauge observations is different (i.e., archived radar imagery was available every 8–9 min while gauge data were available every 5 min), the pairings are irregular in time. Thus, each radar frame is paired with the gauge observation that most closely followed the radar time stamp (e.g., if the radar image showed data for 1018 UTC, the gauge observation taken at 1020 UTC would be matched with that particular image). For radar images that shared a time stamp with a gauge observation, the gauge reading that occurred 5 min after the radar time stamp is used in an effort to account for a time lag between the rotational behavior aloft and the surface precipitation.

After pairing the radar and surface rainfall observation time stamp, each image is subjectively classified into one of two categories, "rotation images" or "nonrotation images," based on the appearance of the KHGX reflectivity and velocity data within each ~33 km × 33 km domain. Embedded rotation was permitted to occur anywhere within the image domain and did not necessarily have to be directly located over the gauge site. To mitigate human error as much as possible, each image is analyzed at least three times. To be conservative with identifying rotation, images where the embedded rotation signatures in the velocity products were weak or located on the cusp of the domain and/or in areas with weak reflectivity returns (<~20 dBZ) are classified as nonrotation images. An example of a rotation versus a nonrotation image is shown in Fig. 8.

The rainfall rates associated with the rotation versus the nonrotation images are compared using basic statistics, and these differences are tested for significance using the Wilcoxon signed-rank test. This statistical test is appropriate for our analysis because it can be used to compare the two distributions of

[1] Hourly rainfall rates are defined as observations beginning at the top of an hour and ending at the bottom of an hour (e.g., 0000–0100 UTC).

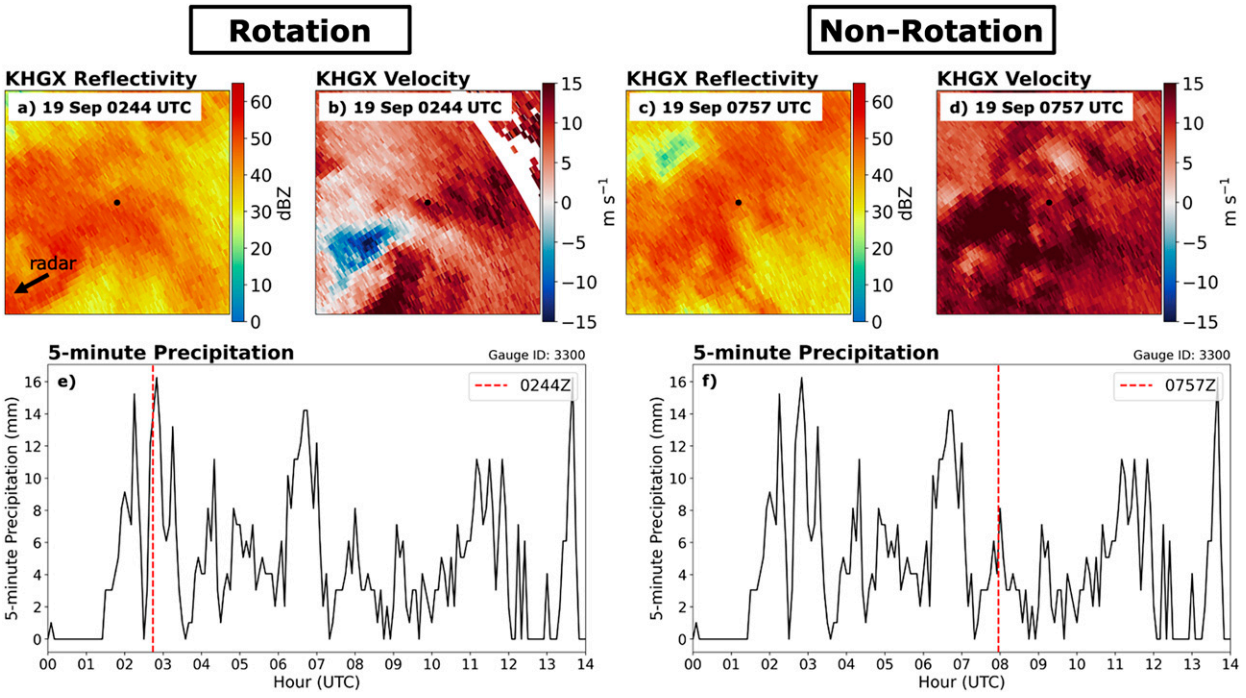

FIG. 8. Example of a rotation image showing embedded rotation within convective precipitation based on (a) reflectivity and (b) storm-relative velocity from the Houston–Galveston radar (KHGX) at gauge site 3300 in the Jefferson County gauge network at 0244 UTC 19 Sep. This is contrasted with (c) KHGX reflectivity and (d) storm-relative velocity for a nonrotation image at the same gauge site. The black dot in the center of (a)–(d) is the gauge site, and the location of the radar relative to the gauge site is shown in (a). (e),(f) The 5-min precipitation observations from the gauge site (black line) with the time of the radar images corresponding to (a) and (b) in (e) and (c) and (d) in (f), annotated as a red dashed line.

nonparametric, independent[2] data (Wilcoxon 1946; King and Eckersley 2019), which are both true of our data. In essence, the Wilcoxon signed-rank test takes the differences between paired data, ranks the positive and negative differences (separately) according to the absolute value of the magnitude of those differences. The sum of the positive ranks is used to calculate the test statistic using the following equation:

$$z = \frac{w - \frac{N(N+1)}{4}}{\sqrt{\frac{N(N+1)(2N+1)}{24} - t}} = \frac{w - \mu}{\sigma - t}, \qquad (2)$$

where z is the test statistic, w is the sum of the positive ranks, N is the number of pairs with a nonzero difference, μ is the mean, σ is the standard error, and t is a correction factor for tied ranks.

Because the number of rotation images and number of nonrotation images are not equal, the mean test statistic and mean p value of 100 000 randomized pairs[3] of rainfall observations following rotation and nonrotation images are computed, with each sample of pairs being equal to the length of the shorter dataset (which happens to be the rainfall observations following the nonrotation images). Using a significance level of $\alpha = 0.01$ in this one-sided test, the null hypothesis is that the median of the differences between the precipitation observations following the rotation images and those following nonrotation images is less than zero (i.e., more rain fell after nonrotation images, rather than after rotation images), and the alternative hypothesis is that this difference is positive.

The basic statistics and Wilcoxon signed-rank test are performed twice: once for the full set of rainfall observations following all 1067 radar images and once for a smaller dataset, where the 5-min precipitation observations that reported zero rainfall are removed ($n = 859$). Hereafter, the former dataset will be referenced as "all_data," and the latter will be referred to as "no0_data."

d. *Horizontal distance dependency between rotation and rainfall rates*

To further expand the subjective analysis portion of the study, the relationship between horizontal distance between the radar-identified rotation and the amount of rain that fell at nearby gauges is examined. A smaller time period within Imelda is used to explore this theory, and the goal is to

[2] The results section illustrates that the data are nonparametric, and independence is validated by performing the Mann–Whitney U test (an analogous test that assumes non-independence) on the dataset: this test yielded greater statistical significance than the Wilcoxon signed-rank test, implying that independence was a conservative assumption.

[3] This number of samples produced results that were nearly identical across multiple random seeds.

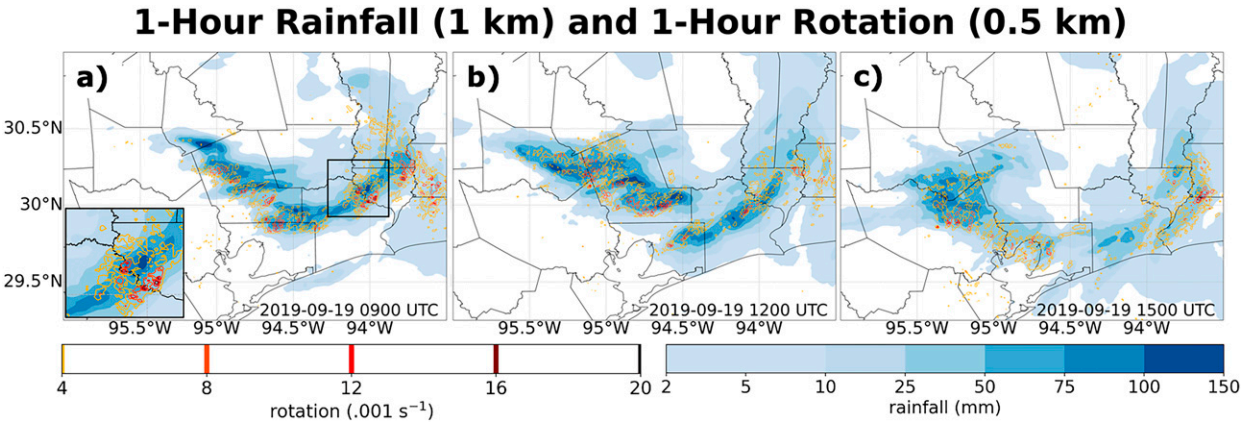

FIG. 9. Examples of the overlaid (noncoarsened) Multi-Radar Multi-Sensor (MRMS) 1-h quantitative precipitation estimate (QPE; shaded; mm) and area-averaged MRMS 1-h accumulated 0–2-km rotation track (contoured) products at (a) 0900, (b) 1200, and (c) 1500 UTC 19 Sep. In (a), the inset figure on the bottom left illustrates a zoomed-in portion of the main figure, which is outlined by the black box.

investigate two aspects of this distance dependency. First, changes in the 5-min rainfall rates across varying horizontal distances from the center of an embedded rotating feature are examined. Second, the effects that constraining the distance threshold between the gauge site and the center of rotation have on the magnitude of the relationship between rotation and rainfall rates are explored.

First, radar reflectivity and velocity are used to subjectively identify the approximate center of one of the long-lasting rotating features that occurred between 0152 and 0326 UTC 19 September (according to the radar time stamps). This time frame is selected for two reasons. First, this roughly 90-min time period was within the 14-h period of intense rainfall that is used in the broader radar and rain gauge analysis described above, so the processes that were evident on radar at that time were already familiar. Second, 10 of the 11 Jefferson County gauges that the 5-min data are pulled from were considered to be associated with rotation for that entire period based on the first analysis: this factor allows for rotation to be held constant while varying only the distance between the gauge and the rotation center and also offers comparison of a large number of gauges over the same time period.

As was done with the larger subjective radar and rain gauge analysis, the 5-min gauge observations that most closely followed the radar time stamp are paired with each radar image (i.e., gauge readings between 0155 and 0330 UTC). For each radar time stamp, the horizontal distance between each of the 10 gauge sites and the approximate rotation center on radar are calculated. This process yielded 120 values (i.e., 12 observation periods of 5 min each paired with the radar images across 10 gauge sites) that are used to compare rainfall amounts versus distance of the gauge from the center of rotation.

For the second portion of this part of the study, a sensitivity analysis on the horizontal distance threshold between gauge and rotation for differentiating between rotation images and nonrotation images is conducted. The objective is to examine how the relationship between rotation and rainfall changes depending on how large of a constraint is placed on the distance between them. To do so, the 1-h precipitation rates that were recorded across all 72 Jefferson County gauge sites between 0200 and 0300 UTC 19 September—a time frame that is encapsulated by the 90-min period described above—are examined. During this period, the mean location of the center of the rotating feature of interest is calculated across the radar images, and then the distance between the mean rotation center and each of the gauge sites is determined. From there, eight different thresholds are applied to test the sensitivity of the distance for which a gauge is considered to be near rotation or not. The horizontal distance thresholds tested are 2, 4, 7, 10, 16.5, 20, 25, and 35 km—i.e., four smaller and three larger thresholds than the one used in the full radar and rain gauge analysis (which was 16.5 km for the 33 km × 33 km boxes and is also tested here). For each threshold, gauges that are closer to the mean center of rotation than the threshold are considered to be associated with rotation images whereas gauges that are further from the mean rotation center are grouped with nonrotation images. The differences in the amount of rain that fell with rotation versus without rotation are examined across the different thresholds.

4. Results and discussion

a. *MRMS analysis*

1) SPATIAL TRENDS

Overlaying the hourly MRMS radar-gauge QPE and rotation tracks suggests that throughout the 18-h period, areas with high rotation track values tended to occur close to areas of locally heavy accumulated rainfall (Fig. 9). Many of these rotating features remained over the same locations for several hours as extreme rainfall rates continued. These two variables tended to be maximized in two locations: one within the north–south-oriented bowing structure near the Texas–Louisiana

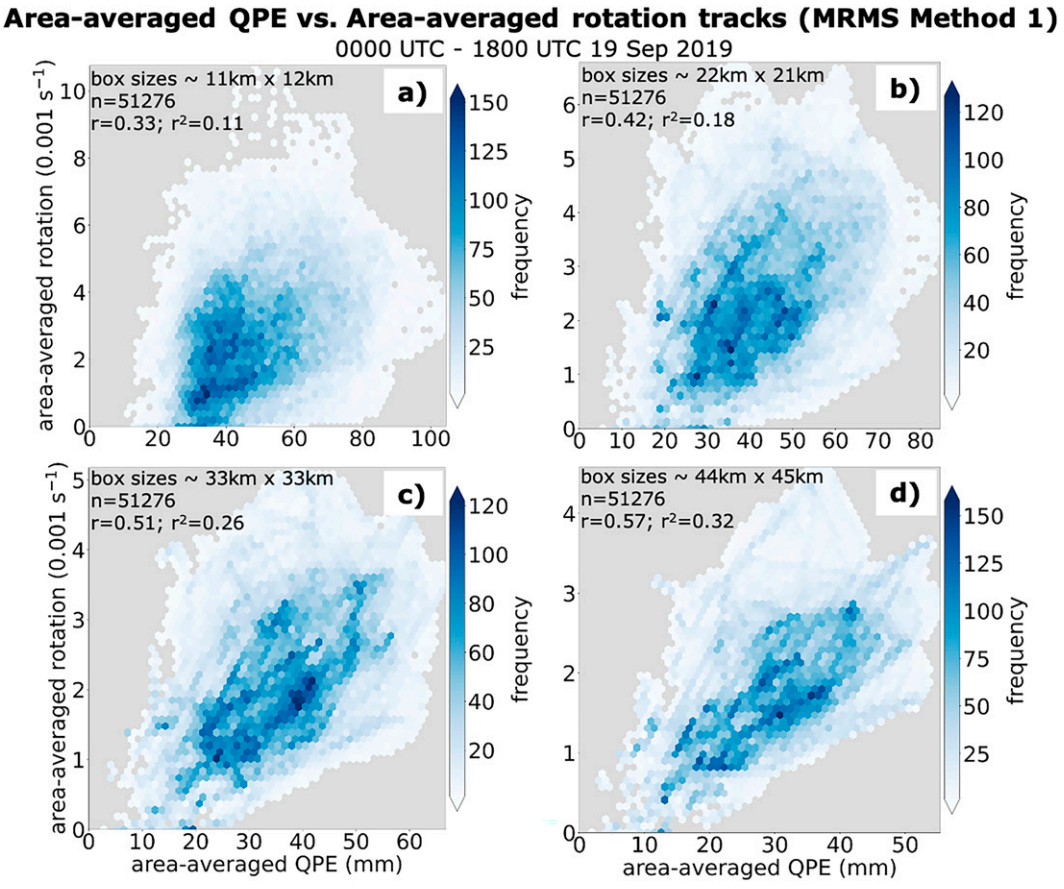

FIG. 10. Two-dimensional histograms of area-averaged Multi-Radar Multi-Sensor (MRMS) 1-h local gauge bias-corrected quantitative precipitation estimate (QPE; mm) and area-averaged MRMS 1-h accumulated 0–2-km rotation tracks calculated from horizontal domains of approximate sizes of (a) 11 km × 12 km, (b) 22 km × 21 km, (c) 33 km × 33 km, and (d) 44 km × 45 km as described by MRMS method 1. Note the differences in scale on the color bars and axes. The number of horizontal domains being sampled (which is based on the number of QPE grid points that are greater than 32 mm h^{-1}) are annotated with the r and r^2 values for each domain size.

border and the other in the back-building line in the form of multicellular structures.

2) SPATIAL CORRELATIONS

Beginning with MRMS method 1, 51 276 total grid cells exceed 32 mm h^{-1} in the 1-h MRMS radar-gauge QPE product within the established spatiotemporal domain. The two-dimensional histograms of the area-averaged hourly MRMS radar-gauge QPE and area-averaged MRMS rotation tracks show a positive correlation between the two variables (Fig. 10). This relationship is present regardless of the sizes of the averaging boxes that are used to conduct the spatial averaging, though as the size of the averaging boxes increases, the correlation coefficient r also increases. This is not surprising, given that as the averaging boxes become larger in size, there is more overlap between the boxes, so the spatial averages calculated among them become more similar. When the smallest averaging box size, 11 km × 12 km, was used, most of the averaging boxes had an area-averaged radar-gauge QPE value between 25 and 60 mm h^{-1} and an area-averaged rotation track value between 0.5 × 0.001 and 4.5 × 0.001 s^{-1} (Fig. 10a). When this smallest averaging box size is used, the range within which the greatest density of area-averaged values fall within the two-dimensional distribution is not highly linear (consistent with the positive, but relatively small r value, Fig. 10a), but the linearity does become more apparent as the averaging box size is increased (Figs. 10b–d).

As the size of the averaging boxes increases, the magnitudes of the spatially averaged MRMS radar-gauge QPE and MRMS rotation tracks become less extreme (Fig. 10). This trend exists because the isolated extreme values begin to get averaged-out as additional, less extreme grid points are averaged together. This result is evident in the correlation coefficients, with the r values of the averaging boxes of size 11 km × 12 km, 22 km × 21 km, and 33 km × 33 km being 0.33, 0.42, and 0.51, respectively. By the time the box size is ~44 km × 45 km (Fig. 10d), an r value of 0.57 is reached, and the maxima of the area-averaged MRMS radar-gauge QPE and area-averaged MRMS rotation tracks are approximately 55 mm h^{-1} and 4.5 × 0.001 s^{-1} respectively, which were characterized more

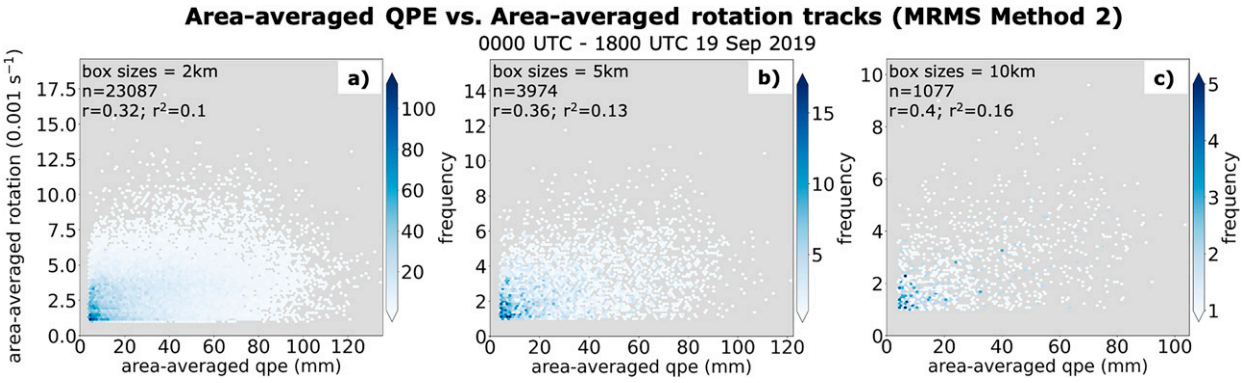

FIG. 11. Two-dimensional histograms of area-averaged Multi-Radar Multi-Sensor (MRMS) 1-h local gauge bias-corrected quantitative precipitation estimate (QPE; mm) and area-averaged MRMS 1-h accumulated 0–2-km rotation tracks calculated from coarsened grids with horizontal resolutions of (a) 2, (b) 5, and (c) 10 km as described by MRMS method 2. Only coarsened grid boxes that have an area-averaged 1-h QPE greater than 4 mm and an area-averaged 1-h accumulated rotation track greater than 0.001 s^{-1} are included. Note the differences in scale on the color bars and axes.

as midrange values when the averaging boxes were smaller (e.g., Fig. 10a).

Analyzing the results of the MRMS method 2 reveals that there is still some positive relationship between the area-averaged MRMS rotation tracks and the area-averaged MRMS radar-gauge QPE, though the correlations are much weaker than those that were found with MRMS method 1 (Fig. 11). As with the first method, the correlation between the area-averaged MRMS QPE and area-averaged MRMS rotation tracks increases as the grid becomes coarser: using this approach yields r values of 0.32, 0.36, and 0.4 for averaging box sizes of 2 km × 2 km, 5 km × 5 km, and 10 km × 10 km, respectively. Because the oversampling issue is alleviated with MRMS method 2, it is not surprising that these relationships are not as prevalent, since the values of the averaging boxes being analyzed with this second method will undoubtedly be less similar to each other.

The results of the statistical significance testing show that all mean calculated critical values were statistically significant at the $p = 0.01$ level, except for the 2 km × 2 km and 11 km × 12 km averaging boxes (which had critical values of 0.02 and 0.012, respectively; Table 1). Thus, these values indicate that for the majority of the averaging boxes, the null hypothesis would be rejected, suggesting that there is some correlation between the MRMS radar-gauge QPE and the MRMS rotation tracks. The mean critical values quickly become smaller as the averaging box size increases. For instance, the critical values associated with the largest averaging box sizes are several orders of magnitude smaller than those that were calculated for the smaller averaging boxes (e.g., 2.79×10^{-5} for the 33 km × 33 km averaging boxes and 2.87×10^{-6} for the 44 km × 45 km averaging boxes). Thus, the magnitudes of the critical values seem to reflect the strength of the linear relationship between the MRMS radar-gauge QPE and the MRMS rotation tracks, which varied across averaging box sizes.

TABLE 1. Mean correlation coefficient and mean critical values across 1000 iterations (for MRMS method 1 averaging boxes) and 10 000 iterations (for MRMS method 2 averaging boxes).

Averaging box size	MRMS method	Mean correlation coefficient	Mean critical value
2 km × 2 km	2	0.32	0.02
5 km × 5 km	2	0.36	0.009
10 km × 10 km	2	0.4	0.003
11 km × 12 km	1	0.33	0.012
22 km × 21 km	1	0.42	0.0015
33 km × 33 km	1	0.51	2.79×10^{-5}
44 km × 45 km	1	0.57	2.87×10^{-6}

While there are similarities among the results of the two methods, there are a few notable differences. For one, it appears that the majority of the area-averaged values are centered in the lower left-hand corner of the plots for MRMS method 2 (Fig. 11), demonstrating that the majority of the area-averaged QPE and area-averaged rotation values tended to be relatively small. These smaller values are responsible for much of the strong positive correlation, for the data become less correlated as smaller values are removed (not shown). Additionally, MRMS method 1 shows a clear absence of high area-averaged QPE/low area-averaged rotation (and vice versa), suggesting that some amount of rotation was always present when the most extreme area-averaged rainfall occurred. However, this feature is not prevalent in the plots associated with MRMS method 2, which limits the validity of that finding.

To summarize, while both averaging approaches suggest some positive association between area-averaged QPE and area-averaged rotation in the MRMS data captured during Imelda, the magnitude of the relationship between these two variables is not consistent among the two methods. First, MRMS method 1 suggests that on multiple spatial scales, there is a well-defined, positive correlation between low-level rotation and rainfall rates on hourly time scales in Tropical Storm Imelda. This finding is consistent with the relationships gleaned between mesoscale rotation and rainfall in other radar observation-based datasets (e.g., Brauer et al. 2020; Nielsen and Schumacher 2020a).

TABLE 2. Cross tabulation of 5-min rainfall observations following nonzero precipitation images (no0_data), zero precipitation images, and all images (all_data) based on whether or not the image contained subjectively identified rotation. Row-wise and column-wise percentages are also computed against the total number of images.

	Nonzero images	Zero images	All images
Rotation images	525	91	616
(row %)	(85.23%)	(14.77%)	(100%)
(column %)	(61.12%)	(43.75%)	(57.73%)
Nonrotation images	334	117	451
(row %)	(74.06%)	(25.94%)	(100%)
(column %)	(38.88%)	(56.25%)	(42.27%)
Total images	859	208	1067
(row %)	(80.51%)	(19.49%)	(100%)
(column %)	(100%)	(100%)	(100%)

While the findings from MRMS method 2 do not contradict this relationship, they do imply a much weaker relationship between rotation and rainfall, which raises questions as to how significant that association is. Second, the results using MRMS method 1 suggest that strong area-averaged values of either rotation or rainfall rates do not tend to be present without moderate to strong values of the other, indicating that there may be some amount of codependency between extreme values of these variables. However, this relationship was not present in the dataset when MRMS method 2 was applied, which illuminates the need to investigate further.

b. *Radar and rain gauge analysis*

1) SUBJECTIVE ANALYSIS

When all 1067 subjectively analyzed radar images (all_data) are considered, 616 radar images (57.73%) were found to have rotation while 451 (42.27%) were determined to have no rotation present (Table 2). Of these 1067 images, approximately 20% (208) of the 5-min rainfall observations associated with them show records of zero precipitation, 91 of which were associated with rotation and 117 without. In almost all cases, these recordings of zero precipitation were not because there was no hydrometeor-related reflectivity present in the domain around the gauge site, but rather it was because either 1) the precipitation did not occur right over the gauge or 2) the temporal mismatch between the radar image and gauge observation "missed" when the rain fell. Removing images associated with precipitation observations of zero leaves 525 rotation images and 334 nonrotation images that recorded nonzero 5-min rainfall observations, which represent 61.12% and 38.88% of no0_data, respectively (Table 2).

Examining the 5-min rainfall observations for all_data shows that the mean and median precipitation observed after rotation images are 5.1 and 4.1 mm, respectively, which are approximately 1–1.5 mm higher than the rainfall following nonrotation images in all_data (Figs. 12a,b). Both distributions are strongly skewed right, showing that most of the 5-min precipitation observations in the dataset are small, while the more extreme readings are rarer. Boxplots confirm this assessment: approximately 75% of the observations fall at or below 8 mm for the rotation images compared to 5 mm for the nonrotation images (cf. Figs. 12a,b). The observations following nonrotation images are heavily weighted by the zero observations, as shown by the 25th percentile value of 0 mm. Meanwhile on the upper end of the distributions, the most extreme precipitation rates tended to occur after rotation images rather than nonrotation images. In fact, the outlier observations following nonrotation images actually fall within the 90th percentile of observations following rotation images (which is approximately 16 mm).

When "zero" observations are removed (no0_data), the right-skewness is still apparent in both distributions of rainfall observations following rotation and nonrotation images (Figs. 12c,d). Removing observations of 0 mm reduces the standard deviation slightly for the distributions of observations that follow rotation and nonrotation images compared to when those observations were included (cf. Figs. 12a,c,b,d). This is also evident in the shrinking of the interquartile ranges, which results from the 25th percentile increasing and the 75th percentile decreasing.

Though the magnitude of the differences in the observations following rotation images and the observations following nonrotation images may appear small, these differences become much more important when they are compounded over time. Over the 14-h period, the 5-min rainfall accumulations that were analyzed alongside the radar images totaled approximately 4662 mm across the 11 gauges. Of this total precipitation, 3131 mm of it fell in the minutes after embedded rotation occurred. In other words, over two-thirds of the rainfall that was included in the analysis fell when rotation was identified in close proximity to the gauge. Even when scaled by the number of observations, the total precipitation following rotation images was 1914 mm, compared to 595 mm for the total rainfall following nonrotation images, further emphasizing that rain rates tended to be higher when rotation was present.

In general, the rotation-associated rainfall rates recorded by the Jefferson County gauges appear to be comparable to rain rates that have been documented by gauges during continental convection with rotating storm-scale features. For instance, Smith et al. (2001) described two supercell cases, one in Orlando, Florida, and one in Dallas, Texas, where gauges recorded maximum rainfall rates of 222 and 231 mm h^{-1} on 5-min time scale, respectively. These rates are very close to the maximum 5-min rain rate of approximately 244 mm h^{-1} that was recorded by a gauge site during Imelda. On hourly time scales, maximum gauge-recorded rain rates across different supercell cases have varied quite a bit, from 75 mm h^{-1} up to over 140 mm h^{-1} (e.g., Doswell 1998; Smith et al. 2001; Nielsen and Schumacher 2020a), the upper end of which is comparable to Imelda's hourly gauge maximum of 165 mm h^{-1}. We can also compare these gauge-recorded rain rates to the Tax Day (2016) flooding event: a nontropical cyclone event that was captured in part by the Harris County, Texas, rain gauge network that was alluded to previously (Nielsen and Schumacher 2020b). Unlike the aforementioned supercell cases, the Tax Day flooding event featured a mesoscale convective system

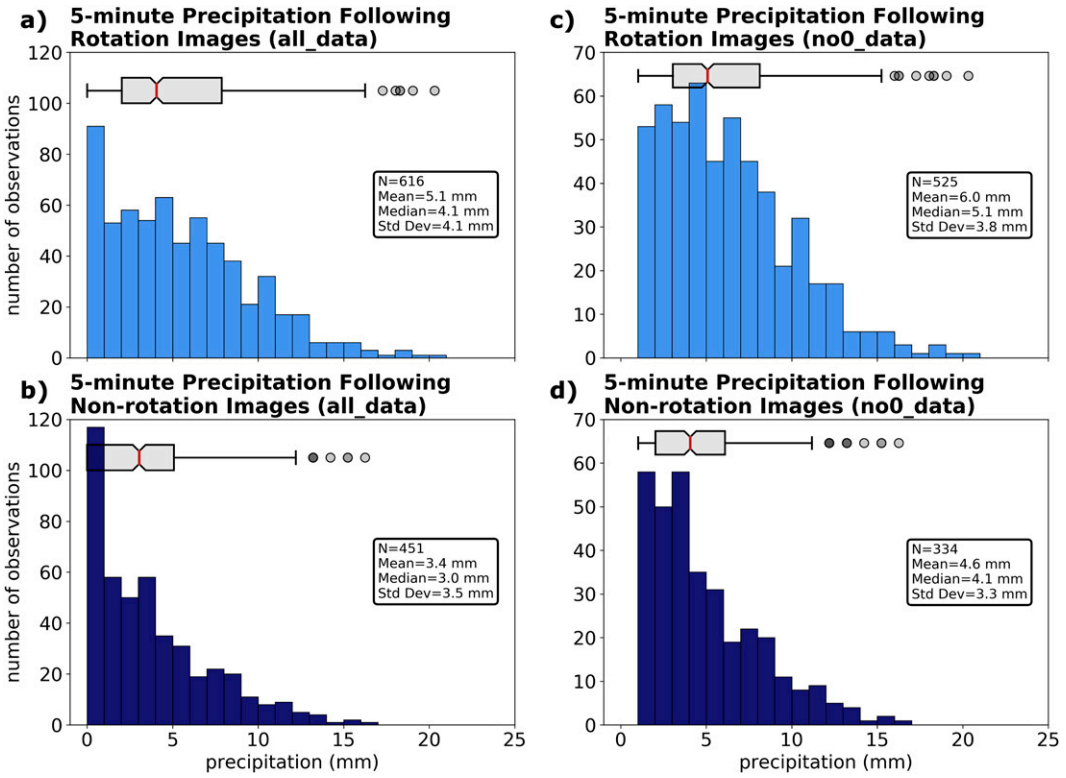

FIG. 12. Histograms and boxplots showing the distribution of 5-min precipitation values from 11 Jefferson County, TX, gauge sites in the minutes following radar images (a),(b) when all images are considered and (c),(d) when images that precede nonzero rainfall observations are removed. (top) The 5-min precipitation accumulations that follow images containing rotation and (bottom) the 5-min accumulations when nonzero observations are removed. Basic statistics for each distribution are also annotated. Note the differences in scale on the *y* axes.

with embedded rotating features, which draws similarities to Imelda. In their study, Nielsen and Schumacher (2020b), showed that a maximum rain rate of 328 mm h^{-1} (on a 5-min time scale) was captured by the gauge network during that event, and while this value is obviously larger than the gauge-maximum recorded during Imelda, the widespread 5-min rain rates of 60–120 mm h^{-1} that were captured during the 2016 Tax Day flood are very comparable to the 5-min rain rates documented by the gauges during Imelda.

In general, while the findings show that the 5-min rainfall observations taken during Imelda did not individually differ much between when rotation was present versus not, the small differences accumulated quickly over time, illustrating that rotation may have played a significant role in enhancing surface rainfall. This finding is consistent with previous work involving modeling, which have shown that mesoscale rotation can locally increase rainfall rates through dynamic processes (e.g., Nielsen and Schumacher 2018, 2020b). It also agrees with observational studies that have identified positive associations between rainfall rates and mesoscale rotation on hourly time scales (e.g., Brauer et al. 2020; Nielsen and Schumacher 2020a,b).

2) STATISTICAL SIGNIFICANCE

The mean of the positive rank sums (w) calculated from the 100 000 random-paired samples are approximately 56 900 and 30 500 for all_data and no0_data, respectively, and their distributions are shown in Fig. 13. Following the methods of the Wilcoxon signed-rank test, we use this distribution of positive rank sums to test the significance of the data by calculating the mean test statistics (z) with Eq. (2) by taking the means of means (μ) and mean standard errors (σ) according to the mean number of nonzero paired differences (N) for the 100 000 samples taken from all_data and no0_data.

The results of the test show that the null hypothesis can be rejected in both all_data and no0_data. That is, there is significant evidence in both datasets to support the claim that the median of the differences between the rainfall rates following the rotation images and the rainfall rates following the nonrotation images is not negative: more rain tended to fall when rotation existed. To expand further, the significance test places the means of the positive ranks at approximately 6.4σ (for all_data) and 4.8σ (for no0_data) above μ in the distributions of rank sums (Fig. 13), which corresponds to p values of approximately 6×10^{-6} and 1×10^{-9} for no0_data and all_data, respectively (Table 3). These p values are much smaller than the critical value of 0.01, which leads to the rejection of the null hypothesis. As such, the results of the Wilcoxon signed-rank test are consistent with the alternative hypothesis: the median of the signed paired differences is not less than zero, but rather, is greater than zero. This finding

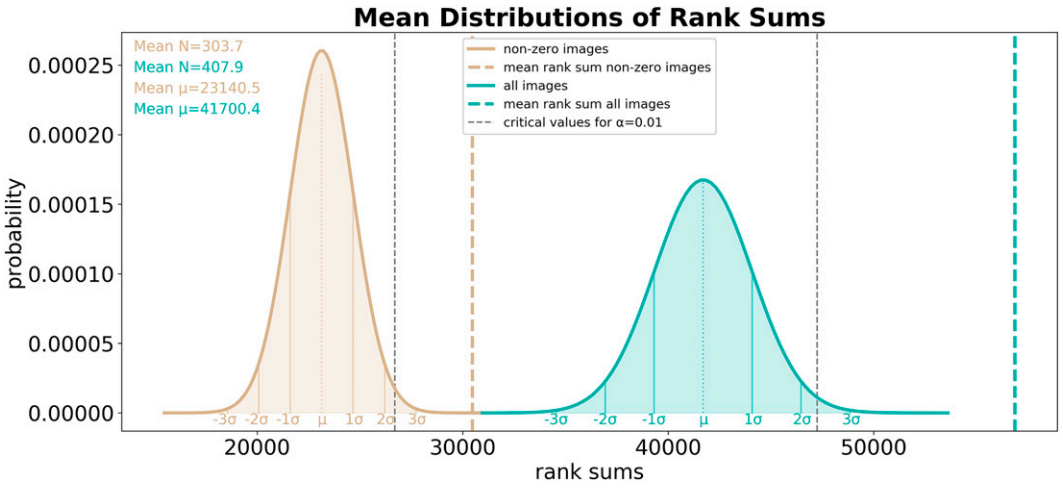

FIG. 13. Mean probability distributions of the positive rank sums using a normal approximation based on the mean of means and mean of standard deviations from the 100 000 randomly paired rainfall observations following rotation and nonrotation images for all images (all_data, turquoise) and nonzero images only (no0_data, tan). Distributions are shown for ±5 mean standard errors (σ), with $\pm 3\sigma$ shaded and labeled. The mean of means μ is also noted as dotted lines and annotated in the top-left corner with the mean number of nonzero pairs (N) determined through the 100 000 random pairs that were analyzed. The critical rank sum values corresponding to a significance of $\alpha = 0.01$ are shown as gray dashed lines. The mean rank sum values corresponding to the mean test statistics from the 100 000 random pairs are shown as tan and turquoise dashed lines for no0_data and all_data, respectively. Note μ and σ are calculated using Eq. (2).

suggests that in the data, there is a significant positive difference in the 5-min gauge rainfall for observations that follow rotation versus those that do not follow rotation, regardless of whether zero precipitation values are included or not.

3) DISTANCE DEPENDENCY OF ROTATION AND RAINFALL

Examining the 5-min rainfall rates of the 10 Jefferson County gauges versus their distance from the approximate center of the rotating feature over the roughly 90-min period on 19 September suggests a weak negative relationship between the two variables, with an r value of −0.24 (Fig. 14). That is, there is a subtle indication that rain rates tended to be greater when the gauge site was located closer to the center of the rotating feature, but the signal is quite weak. The majority of the rain rates on the far upper end of the distribution (e.g., greater than 10 mm in 5 min) did occur at relatively short distances from the approximate center of the embedded rotation (Fig. 14), but there are also several very low rain rates (e.g., less than 4 mm in 5 min) that were also within only a few kilometers of the center of the rotating feature. This pattern in the most extreme rainfall rates detected in Imelda is consistent with both the results from MRMS analysis and the subjective radar and rain gauge analysis.

When the 5-min rain rates from the 10 gauges are aggregated over the 0155–0330 UTC period, the strength of the negative relationship between distance and total precipitation increases (according to the calculated r value of −0.67, not shown). This finding builds on our previous analysis to suggest that rainfall rates not only compound quickly over time, but when rotation is very close to the gauge site, the effect may be even more profound.

Last, testing the sensitivity of the threshold for the horizontal distance between the gauge and the center of the rotating feature of interest for the 0200–0300 UTC 19 September period yields interesting results. Increasing the distance threshold by just a few kilometers very quickly increases the number of gauges that are considered to be associated with rotation, as is evidenced by this value more than tripling when the threshold is increased from 4 to 10 km (Fig. 15a). Comparing the means of the 1-h precipitation rates associated with

TABLE 3. Mean values of the sum of the signed ranks (rounded to the nearest 100), mean test statistics (calculated from the mean sum of positive signed ranks), and corresponding mean p values resulting from the 100 000 random pairs of rainfall observations following rotation images and nonrotation images when all images (all_data) and only nonzero images are analyzed (no0_data).

	Mean sum of positive signed ranks	Mean (absolute value) sum of negative signed ranks	Mean Wilcoxon signed-rank test statistic	Mean p value
All images	56 900	26 500	6.4	1×10^{-9}
Nonzero images only	30 500	15 800	4.8	6×10^{-6}

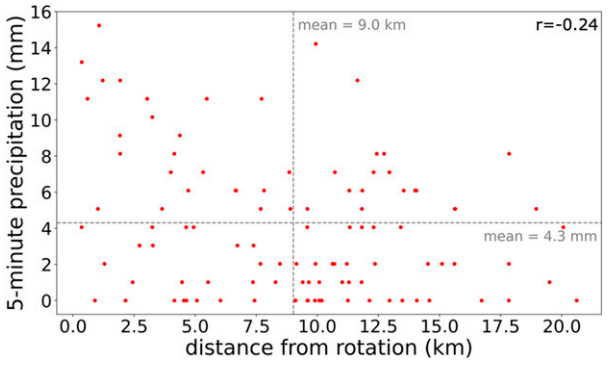

FIG. 14. Distance of the gauge site from the center of the rotating feature vs 5-min precipitation rates for 10 Jefferson County gauges across radar time stamps 0152–0326 UTC 19 Sep 2019. Mean distances between the gauge and center of rotation, mean 5-min precipitation rates, and the *r* value representing the correlation coefficient are annotated.

rotation to the means of the 1-h precipitation rates associated with no rotation over the varying distance thresholds shows that the biggest differences tend to occur when the threshold was very small (Fig. 15b). This slope seems to be evident both when zero rainfall observations were included as well as when they were excluded. It is also worth noting that by the time the threshold reaches 10 km or larger, the difference between gauges associated with rotation versus gauges not associated with rotation changes very little.

Together, while the analysis period is short, these results suggest that there may be some nonlinear distance dependency with regards to the horizontal radius of influence that embedded rotation may have on precipitation rates within a larger convective system. They also suggest that these rainfall enhancements may be greatest over distances of only a few kilometers or less. However, more work is needed to quantify how wide the horizontal distances are over which rotation can influence rainfall rates, and other factors that may affect this relationship should also be explored (e.g., the horizontal extent of the rotation, the magnitude of the rotation, the convective mode, etc.).

c. *Limitations*

There are a few limitations with this study that should be addressed, beginning with the downsides of using only one LTC in these analyses. Because this is a case study, broader generalizations about observations of embedded rotation and extreme rainfall in LTCs cannot be made. Moreover, Tropical Storm Imelda was a relatively weak, short-lived TC, and its most extreme rainfall occurred when the system had been reduced to remnants. This means that while the relationship between embedded rotation and rainfall rates shown here may translate to other LTCs that evolve into disorganized remnants, the relationship of these two mechanisms in LTCs with better-developed structures remains outside the scope of this work.

There are also some aspects of our methods that are worthy of discussion. In the analysis involving the MRMS data, one area of concern involves autocorrelation between the area-averaged MRMS rotation tracks and MRMS radar-gauge QPE values over time. While some autocorrelation should be expected, this topic presents a limitation, particularly when overlaps are permitted among the averaging boxes. Additionally, while the precipitation threshold used in this study was informed by previous observational studies on heavy rainfall [viz., the threshold's relationship to average recurrence intervals and urban flooding, see Nielsen and Schumacher (2020a)'s methods for more details], adjusting this value can yield different results. For instance, setting the threshold too high introduces a smaller sample size (and in general reduces the relationship between the two variables). On the other hand, setting the threshold too low enhances the effects of zero precipitation values that extend beyond the small rainfall rates that are typically on the

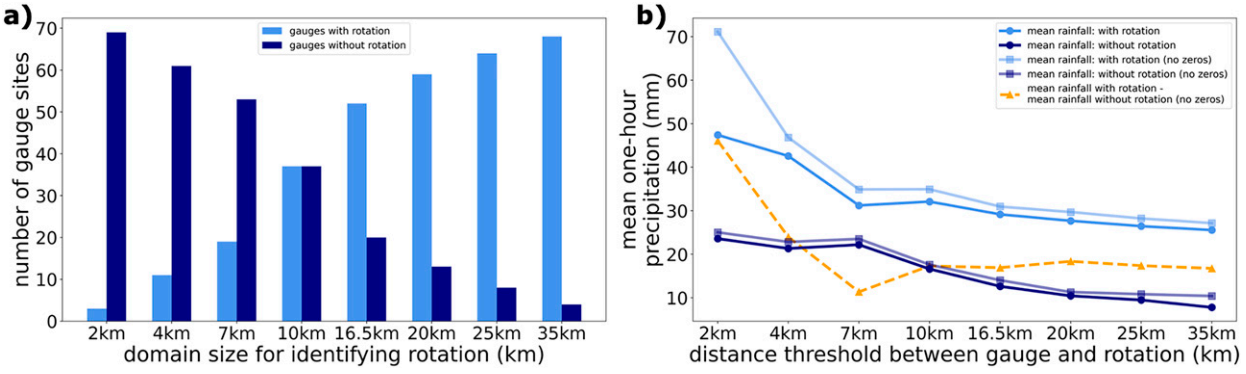

FIG. 15. During the 0200–0300 UTC 19 Sep period, (a) number of gauges associated with rotation (light blue) vs number of associated with nonrotation (navy blue) based on varying horizontal distance thresholds, and (b) mean 1-h precipitation for gauges with rotation (light blue with circle markers) and mean 1-h precipitation for gauges without rotation (navy blue with circle markers) across varying horizontal distance thresholds. In (b), the mean values of 1-h precipitation with and without rotation at varying horizontal thresholds are also shown when zeros are removed (lightest blue with square markers and lighter navy with square markers for rotation and nonrotation, respectively). The orange dashed line in (b) shows the difference between the nonzero mean precipitation with rotation and nonzero mean precipitation without rotation.

periphery of precipitating systems; this introduces more zero rainfall/zero rotation values and likely overestimates the relationship between the two processes.

A final limiting aspect of this work involves the time scales associated with the paired radar images and the 5-min rainfall observations. Our methods weighted observations that occurred anywhere between 1 and 5 min after the radar image equally. As a result, some 5-min observation periods for the precipitation may have begun several minutes before the time of the radar image, while others may have occurred entirely after the radar image was captured. Additionally, some 5-min observations were neglected entirely if they fell between certain radar time stamps (e.g., the 0225 UTC gauge observation would be neglected for radar scans occurring at 0218 and 0226 UTC). While our analysis using a 5-min temporal resolution is an improvement from the hourly time scales used in previous work on this topic (e.g., Brauer et al. 2020; Nielsen and Schumacher 2020a), these issues may complicate the ability to draw comparisons.

5. Summary and conclusions

This study utilized remote data (from radar) and in situ observations (from rain gauges) to evaluate and quantify the relationship between embedded rotation in the lower atmosphere and surface precipitation rates through a case study of Tropical Storm Imelda. Broadly, these findings suggest that in this system, there was a positive, statistically significant relationship between low-level meso- to storm-scale rotation and rainfall rates. That is, more rain tended to fall when there was embedded rotation present in Imelda's convection.

First, in the synoptic and mesoscale analysis, the general evolution of Tropical Storm Imelda was discussed and the ingredients that favored heavy to extreme rain rates in the system's remnants were described. The TC made landfall as a tropical storm on 17 September 2019 along the western Gulf Coast of the United States. The slow-moving system brought moderate rainfall to western coastal Texas and southern Louisiana for roughly 36–48 h. Imelda's remnants then evolved into a quasi-stationary back-building MCS around the start of 19 September, bringing extreme rain rates in excess of 100 mm h^{-1} to a localized area of western Texas, which already had saturated soils from rain that fell over the previous days. These extreme rain rates persisted for several hours, creating localized but impactful flooding in some locations. A combination of the following processes favored this heavy rainfall:

1) sustained ambient moisture from Imelda plus ongoing moisture advection,
2) ample surface-based instability and deep warm cloud depths to favor warm rain processes,
3) a confluent low-level wind field that enhanced vertical wind shear and aided storm organization, and
4) a surface cold pool that served as a mechanical lifting mechanism for vertical forcing for ascent.

In the first analysis that was conducted to examine rotation and rainfall, the 0–2-km rotation track and local gauge bias-corrected radar-estimated 1-h QPE products from the MRMS system were used to investigate the relationship between meso- to storm-scale rotation and rainfall rates. To do so, two spatial-averaging approaches to soften the 0.5–1-km grids to a more appropriate scale (ranging from ~2 km × 2 km to ~44 km × 45 km) were applied over an 18-h period on 19 September. This approach led to three key findings. First, there were several locations with persistent rotating features that lasted on the order of up to several hours and tended to be closely collocated with areas of heavier accumulated rainfall. Second, there was a positive spatial correlation between area-averaged hourly QPE and area-averaged hourly accumulated rotation tracks: a finding that was consistent across multiple spatial scales. Last, our results show that it was uncommon for low values of area-averaged rotation to be collocated with high values of area-averaged QPE (or vice versa), suggesting a codependency between the two variables.

For the second analysis, 5-min rainfall observations from surface gauges were paired with radar images that were subjectively analyzed for rotation (or nonrotation) on spatial scales no larger than 20 km. Of the 1067 radar images that were subjectively analyzed near the 11 gauge sites from 0000 to 1400 UTC 19 September 2019, approximately 58% of the images contained embedded rotation. Basic statistics showed that 5-min rainfall rates that were paired with rotation images tended to be greater on average [by approximately 1 mm $(5\ \text{min})^{-1}$], and the more extreme observations on the upper end of the distribution tended to be associated with rotation images (rather than nonrotation images). Though these differences may appear small in magnitude, they compounded greatly over time: aggregating the 5-min rainfall data included in the analysis showed almost twice as much rain fell when rotation was present compared to when rotation was not present. Using the Wilcoxon signed-rank test, this difference was statistically significant. Last, a brief exploration of the horizontal distance dependency between the rotation rates and the rainfall rates at gauge sites was provided. These results showed a weak negative association between horizontal distance and rainfall rates at the gauges on 5-min time scales. However, when horizontal distance between the gauge and rotation was highly constrained, the rainfall rates tended to be most extreme compared to gauges that were located only slightly further from the rotation center. This analysis expands on the other results in this manuscript to suggest that the positive relationship between rotation in the low-levels and rainfall rates at the surface may be particularly profound over very short horizontal distances.

Collectively, these results are consistent with previous modeling and observational studies that have demonstrated positively correlated physical and quantitative relationships between low-level storm-scale to mesoscale rotation and surface precipitation rates (e.g., Nielsen and Schumacher 2018, 2020a,b; Brauer et al. 2020). This work provides novel contributions to the field by observationally quantifying this relationship on finer spatiotemporal scales in an LTC environment. Future work could aim to apply these methods to other systems, including ones with various translational speeds and/or are more prolific tornado producers, so that comparisons can be made among system type and broader conclusions can be reached.

Other spatiotemporal averaging approaches (such as weighting techniques) and simulations of LTCs and their heavy rain-producing processes via numerical modeling also offer avenues for future research.

Acknowledgments. The authors thank Erik Nielsen for his collaboration and previous work that helped inspire this project. This work was funded through a 1-yr American Meteorological Society Graduate Research Fellowship (sponsored by the NOAA Climate Program Office) and NOAA VORTEX-SE Grant NA18OAR4590308.

Data availability statement. Real-time data from the two precipitation observing networks are available online (Harris County: https://www.harriscountyfws.org/; Jefferson County: https://dd6.onerain.com/). HURDAT2 Best Track data can be accessed via the NHC data archives webpage (https://www.nhc.noaa.gov/data/). NEXRAD Level II radar data and RAP Analysis data can be requested from NOAA/NCEI (https://www.ncdc.noaa.gov/nexradinv/; https://www.ncei.noaa.gov/products/weather-climate-models/rapid-refresh-update). Upper-air sounding data were accessed via the University of Wyoming's web archive (https://weather.uwyo.edu/upperair/sounding.html). MRMS data were locally archived at Colorado State University, and sharing of the data is restricted as outlined in the MRMS Data Sharing Policy (Gourley and Howard 2014).

REFERENCES

Ashley, S. T., and W. S. Ashley, 2008: Flood fatalities in the United States. *J. Appl. Meteor. Climatol.*, **47**, 805–818, https://doi.org/10.1175/2007JAMC1611.1.

Ashley, W. S., 2007: Spatial and temporal analysis of tornado fatalities in the United States: 1880–2005. *Wea. Forecasting*, **22**, 1214–1228, https://doi.org/10.1175/2007WAF2007004.1.

Benjamin, S. G., and Coauthors, 2016: A North American hourly assimilation and model forecast cycle: The Rapid Refresh. *Mon. Wea. Rev.*, **144**, 1669–1694, https://doi.org/10.1175/MWR-D-15-0242.1.

Bluestein, H. B., J. C. Snyder, and J. B. Houser, 2015: A multiscale overview of the El Reno, Oklahoma, tornadic supercell of 31 May 2013. *Wea. Forecasting*, **30**, 525–552, https://doi.org/10.1175/WAF-D-14-00152.1.

Brauer, N. S., J. B. Basara, C. R. Homeyer, G. M. McFarquhar, and P. E. Kirstetter, 2020: Quantifying precipitation efficiency and drivers of excessive precipitation in post-landfall Hurricane Harvey. *J. Hydrometeor.*, **21**, 433–452, https://doi.org/10.1175/JHM-D-19-0192.1.

Burow, D., K. Ellis, and L. Tran, 2021: Simultaneous and collocated tornado and flash flood warnings associated with tropical cyclones in the contiguous United States. *Int. J. Climatol.*, **41**, 4253–4264, https://doi.org/10.1002/joc.7071.

Corbosiero, K. L., and J. Molinari, 2002: The effects of vertical wind shear on the distribution of convection in tropical cyclones. *Mon. Wea. Rev.*, **130**, 2110–2123, https://doi.org/10.1175/1520-0493(2002)130<2110:TEOVWS>2.0.CO;2.

DeHart, J. C., and M. M. Bell, 2020: A comparison of the polarimetric radar characteristics of heavy rainfall from Hurricanes Harvey (2017) and Florence (2018). *J. Geophys. Res. Atmos.*, **125**, e2019JD032212, https://doi.org/10.1029/2019JD032212.

Doswell, C. A., 1998: Seeing supercells as heavy rain producers. Preprints, *14th Conf. on Hydrology*, Dallas, TX, Amer. Meteor. Soc., 73–79.

——, H. E. Brooks, and R. A. Maddox, 1996: Flash flood forecasting: An ingredients-based methodology. *Wea. Forecasting*, **11**, 560–581, https://doi.org/10.1175/1520-0434(1996)011<0560:FFFAIB>2.0.CO;2.

Dougherty, E., and K. L. Rasmussen, 2019: Climatology of flood-producing storms and their associated rainfall characteristics in the United States. *Mon. Wea. Rev.*, **147**, 3861–3877, https://doi.org/10.1175/MWR-D-19-0020.1.

Edwards, R., 2012: Tropical cyclone tornadoes: A review of knowledge in research and prediction. *Electron. J. Severe Storms Meteor.*, **7** (6), https://ejssm.com/ojs/index.php/site/article/view/42.

——, A. R. Dean, R. L. Thompson, and B. T. Smith, 2012: Convective modes for significant severe thunderstorms in the contiguous United States. Part III: Tropical cyclone tornadoes. *Wea. Forecasting*, **27**, 1507–1519, https://doi.org/10.1175/WAF-D-11-00117.1.

——, C. J. Nowotarski, S. Overpeck, and G. R. Woodall, 2018: Tornadoes in Hurricane Harvey: Documentation and environmental analysis. *29th Conf. on Severe Local Storms*, Stowe, VT, Amer. Meteor. Soc., 52, https://ams.confex.com/ams/29SLS/webprogram/Paper348127.html.

Galarneau, T. J., and X. Zeng, 2020: The Hurricane Harvey (2017) Texas rainstorm: Synoptic analysis and sensitivity to soil moisture. *Mon. Wea. Rev.*, **148**, 2479–2502, https://doi.org/10.1175/MWR-D-19-0308.1.

Gao, S., Z. Meng, F. Zhang, and L. F. Bosart, 2009: Observational analysis of heavy rainfall mechanisms associated with severe Tropical Storm Bilis (2006) after its landfall. *Mon. Wea. Rev.*, **137**, 1881–1897, https://doi.org/10.1175/2008MWR2669.1.

——, J. Zhang, D. Li, H. Jiang, and Z. N. Fang, 2021: Evaluation of multiradar multisensor and stage IV quantitative precipitation estimates during Hurricane Harvey. *Nat. Hazards Rev.*, **22**, 04020057, https://doi.org/10.1061/(ASCE)NH.1527-6996.0000435.

Gourley, J. J., and K. W. Howard, 2014: Multi-radar multi-sensor (MRMS) dataset sharing policy. NOAA, 2 pp., https://www.nssl.noaa.gov/projects/mrms/nmq_data_policy_OGCrevised.pdf.

Green, B. W., F. Zhang, and P. Markowski, 2011: Multiscale processes leading to supercells in the landfalling outer rainbands of Hurricane Katrina (2005). *Wea. Forecasting*, **26**, 828–847, https://doi.org/10.1175/WAF-D-10-05049.1.

Habibi, H., R. Awal, A. Fares, and M. Temimi, 2021: Performance of multi-radar multi-sensor (MRMS) product in monitoring precipitation under extreme events in Harris County, Texas. *J. Hydrol.*, **598**, 126385, https://doi.org/10.1016/j.jhydrol.2021.126385.

Henderson, J., E. R. Nielsen, G. R. Herman, and R. S. Schumacher, 2020: A hazard multiple: Overlapping tornado and flash flood warnings in a National Weather Service forecast office in the Southeastern United States. *Wea. Forecasting*, **35**, 1459–1481, https://doi.org/10.1175/WAF-D-19-0216.1.

Hitchens, N. M., and H. E. Brooks, 2013: Preliminary investigation of the contribution of supercell thunderstorms to the climatology of heavy and extreme precipitation in the United States. *Atmos. Res.*, **123**, 206–210, https://doi.org/10.1016/j.atmosres.2012.06.023.

Keene, K. M., and R. S. Schumacher, 2013: The bow and arrow mesoscale convective structure. *Mon. Wea. Rev.*, **141**, 1648–1672, https://doi.org/10.1175/MWR-D-12-00172.1.

King, A. P., and R. J. Eckersley, 2019: Inferential statistics III: Nonparametric hypothesis testing. *Statistics for Biomedical Engineers and Scientists*, A. P. King and R. J. Eckersley, Eds., Academic Press, 119–145, https://doi.org/10.1016/B978-0-08-102939-8.00015-3.

Landsea, C. W., and J. L. Franklin, 2013: Atlantic hurricane database uncertainty and presentation of a new database format. *Mon. Wea. Rev.*, **141**, 3576–3592, https://doi.org/10.1175/MWR-D-12-00254.1.

Latto, A., and R. Berg, 2020: National Hurricane Center tropical cyclone report: Tropical Storm Imelda (17–19 September 2019). NHC Tech. Rep. AL112019, 28 pp., https://www.nhc.noaa.gov/data/tcr/AL112019_Imelda.pdf.

Marinescu, P. J., P. C. Kennedy, M. M. Bell, A. J. Drager, L. D. Grant, S. W. Freeman, and S. C. van Den Heever, 2020: Updraft vertical velocity observations and uncertainties in high plains supercells using radiosondes and radars. *Mon. Wea. Rev.*, **148**, 4435–4452, https://doi.org/10.1175/MWR-D-20-0071.1.

May, R. M., S. C. Arms, P. Marsh, E. Bruning, J. R. Leeman, K. Goebbert, J. E. Thielen, and Z. Bruick, 2021: MetPy: A Python package for meteorological data. Unidata, accessed 12 April 2021, https://doi.org/10.5065/D6WW7G29.

McCaul, E. W., 1987: Observations of the Hurricane "Danny" tornado outbreak of 16 August 1985. *Mon. Wea. Rev.*, **115**, 1206–1223, https://doi.org/10.1175/1520-0493(1987)115<1206:OOTHTO>2.0.CO;2.

——, 1991: Buoyancy and shear characteristics of hurricane-tornado environments. *Mon. Wea. Rev.*, **119**, 1954–1978, https://doi.org/10.1175/1520-0493(1991)119<1954:BASCOH>2.0.CO;2.

——, and M. L. Weisman, 1996: Simulations of shallow supercell storms in landfalling hurricane environments. *Mon. Wea. Rev.*, **124**, 408–429, https://doi.org/10.1175/1520-0493(1996)124<0408:SOSSSI>2.0.CO;2.

Nielsen, E. R., and R. S. Schumacher, 2018: Dynamical insights into extreme short-term precipitation associated with supercells and mesovortices. *J. Atmos. Sci.*, **75**, 2983–3009, https://doi.org/10.1175/JAS-D-17-0385.1.

——, and ——, 2020a: Observations of extreme short-term precipitation associated with supercells and mesovortices. *Mon. Wea. Rev.*, **148**, 159–182, https://doi.org/10.1175/MWR-D-19-0146.1.

——, and ——, 2020b: Dynamical mechanisms supporting extreme rainfall accumulations in the Houston "Tax Day" 2016 flood. *Mon. Wea. Rev.*, **148**, 83–109, https://doi.org/10.1175/MWR-D-19-0206.1.

——, G. R. Herman, R. C. Tournay, J. M. Peters, and R. S. Schumacher, 2015: Double impact: When both tornadoes and flash floods threaten the same place at the same time. *Wea. Forecasting*, **30**, 1673–1693, https://doi.org/10.1175/WAF-D-15-0084.1.

NOAA/National Centers for Environmental Information, 2021a: NCEI storm events database. NOAA, accessed 25 February 2021, https://www.ncdc.noaa.gov/stormevents/.

——, 2021b: U.S. billion-dollar weather and climate disasters, 1980–present (NCEI Accession 0209268). NOAA, accessed 13 July 2021, https://doi.org/10.25921/STKW-7W73.

Nowotarski, C. J., J. Spotts, R. Edwards, S. Overpeck, and G. R. Woodall, 2021: Tornadoes in Hurricane Harvey. *Wea. Forecasting*, **36**, 1589–1609, https://doi.org/10.1175/WAF-D-20-0196.1.

Rogash, J. A., and R. D. Smith, 2000: Multiscale overview of a violent tornado outbreak with attendant flash flooding. *Wea. Forecasting*, **15**, 416–431, https://doi.org/10.1175/1520-0434(2000)015<0416:MOOAVT>2.0.CO;2.

——, and J. Racy, 2002: Some meteorological characteristics of significant tornado events occurring in proximity to flash flooding. *Wea. Forecasting*, **17**, 155–159, https://doi.org/10.1175/1520-0434(2002)017<0155:SMCOST>2.0.CO;2.

Schumacher, R. S., and R. H. Johnson, 2006: Characteristics of U.S. extreme rain events during 1999–2003. *Wea. Forecasting*, **21**, 69–85, https://doi.org/10.1175/WAF900.1.

——, and ——, 2009: Quasi-stationary, extreme-rain-producing convective systems associated with midlevel cyclonic circulations. *Wea. Forecasting*, **24**, 555–574, https://doi.org/10.1175/2008WAF2222173.1.

Shu, S., X. Feng, and Y. Wang, 2018: Essential role of synoptic environment on rainfall distribution of landfalling tropical cyclones over China. *J. Geophys. Res. Atmos.*, **123**, 11 285–11 306, https://doi.org/10.1029/2018JD028842.

Smith, J. A., M. L. Baeck, Y. Zhang, and C. A. Doswell, 2001: Extreme rainfall and flooding from supercell thunderstorms. *J. Hydrometeor.*, **2**, 469–489, https://doi.org/10.1175/1525-7541(2001)002<0469:ERAFFS>2.0.CO;2.

Smith, T. M., and Coauthors, 2016: Multi-radar multi-sensor (MRMS) severe weather and aviation products: Initial operating capabilities. *Bull. Amer. Meteor. Soc.*, **97**, 1617–1630, https://doi.org/10.1175/BAMS-D-14-00173.1.

Spratt, S. M., D. W. Sharp, P. Welsh, A. Sandrik, F. Alsheimer, and C. Paxton, 1997: A WSR-88D assessment of tropical cyclone outer rainband tornadoes. *Wea. Forecasting*, **12**, 479–501, https://doi.org/10.1175/1520-0434(1997)012<0479:AWAOTC>2.0.CO;2.

Wang, C.-C., H.-C. Kuo, R. H. Johnson, C.-Y. Lee, S.-Y. Huang, and Y.-H. Chen, 2015: A numerical study of convection in rainbands of Typhoon Morakot (2009) with extreme rainfall: Roles of pressure perturbations with low-level wind maxima. *Atmos. Chem. Phys.*, **15**, 11 097–11 115, https://doi.org/10.5194/acp-15-11097-2015.

Weather Prediction Center, 2020: Tropical cyclone rainfall maxima. Weather Prediction Center, accessed 26 July 2021, https://www.wpc.ncep.noaa.gov/tropical/rain/tcmaxima.html.

Wilcoxon, F., 1946: Individual comparisons of grouped data by ranking methods. *J. Econ. Entomol.*, **39**, 269–270, https://doi.org/10.1093/jee/39.2.269.

Zhang, J., and Coauthors, 2011: National Mosaic and Multi-Sensor QPE (NMQ) system description, results, and future plans. *Bull. Amer. Meteor. Soc.*, **92**, 1321–1338, https://doi.org/10.1175/2011BAMS-D-11-00047.1.

——, and Coauthors, 2016: Multi-Radar Multi-Sensor (MRMS) quantitative precipitation estimation: Initial operating capabilities. *Bull. Amer. Meteor. Soc.*, **97**, 621–638, https://doi.org/10.1175/BAMS-D-14-00174.1.

——, L. Tang, S. Cocks, P. Zhang, A. Ryzhkov, K. Howard, C. Langston, and B. Kaney, 2020: A dual-polarization radar synthetic QPE for operations. *J. Hydrometeor.*, **21**, 2507–2521, https://doi.org/10.1175/JHM-D-19-0194.1.